

Peridynamics compatible with boundary conditions and its verification in plane elastic problems

M. YU, Z. ZHOU, Z. HUANG

*State Key Laboratory of Mechanics and Control for Aerospace Structures,
Nanjing University of Aeronautics and Astronautics, Nanjing 210016, China,
e-mail: ym0904@nuaa.edu.cn (corresponding author)*

IN THE PERIDYNAMIC (PD) THEORY ESTABLISHED BY SILLING AND HIS COLLABORATES, the equation of motion is incompatible with the traction boundary conditions. In order to impose boundary conditions, a technique used is to set a fictitious boundary layer and transforming traction into a body force. This technique is easy to operate, but it is difficult to adapt to complex boundary constraints. To solve this problem, the new peridynamic governing equations with boundary conditions (PDBC) are introduced and simplified. In PDBC, the influence of the boundary conditions is confined to a boundary layer with finite thickness, by which, the surface correction can be shunned. A nonlinear implicit solver for PDBC is implemented. This solver is used to simulate the plane stress problems. The elastic deformations of a rectangular plate under three different boundary conditions, i.e., traction, displacement and mixed boundary conditions, are solved based on the bond-based and ordinary state-based constitutive models. Comparison of computational results between PDBC, the classical elastic theory and the original PD verifies the applicability and accuracy of PDBC and the implicit algorithm.

Key words: boundary conditions, implicit solver, PDBC, peridynamics, PD equation of motion.



Copyright © 2024 The Authors.

Published by IPPT PAN. This is an open access article under the Creative Commons Attribution License CC BY 4.0 (<https://creativecommons.org/licenses/by/4.0/>).

1. Introduction

PERIDYNAMICS (PD) WAS FIRST PROPOSED BY Silling [1, 2] as a new non-local continuum mechanics theory. Since the PD theory relaxes the requirement of continuity of a displacement field, it becomes relatively friendly to analyze deformation accompanied with evolution of discontinuities caused by damage, fracture and impact failure, which are difficult to analyze in the classical continuum mechanical system. So, it has been promoted rapidly in the past two decades. A peridynamic approach can be considered as a continuum version of molecular dynamics [3], as material particles interact within finite distances through an influence function [3–5]. The range over which a material particle interacts with other material particles around it is called the neighborhood, denoted H_x [2]. The radius δ of H_x is called the 'horizon' [1, 3, 4], which is a model parameter

to measure nonlocality. The interactions become more local with a decreasing horizon, and the PD theory converges to the classical elasticity theory when the horizon approaches zero [6]. The PD theory is sensitive to the horizon and the influence function. Consequently, SELESON and PARKS [5] specifically studied the role of an influence function, and BOBARU and HU [7] discussed the value of the horizon. In the numerical calculation, SILLING suggested the grid spacing Δ being taken as one-third of δ [4, 8].

The PD theory shuns the concepts of strain and stress and only involves relative displacement and internal long-range forces. In the governing equations of PD, a spatial integral of the relative displacement is used to replace the spatial derivative of displacement in the classical theory. As a result, PD does not involve the natural boundary condition, that is traction boundary condition [8]. In order to exert the boundary conditions, Silling suggested a technique of the fictitious boundary layer with thickness δ , [4, 8] by which, the displacement constraint and traction exerted on the boundary surface can equivalently be transferred into the displacement and body force in the fictitious boundary layer. Although good results can be obtained by this technique, it is not natural in physics to transfer the boundary traction into the body force uniformly distributed within the fictitious boundary. More importantly, this technique cannot guarantee that the total angular momentum equilibrium is strictly satisfied, see Appendix A. In order to deal with boundary conditions more naturally, a lot of efforts have been made. For example, MADENCI and DORDUNCU [9, 10] proposed a weak-form governing equations of peridynamics, which permit direct imposition natural boundary conditions. HUANG [11] developed a peridynamic equation of motion with boundary traction, from which, the mixed boundary conditions were deduced. Inspired by [11], the peridynamic equation of motion with boundary traction [12, 13, 45] was further applied to analyze some benchmark problems of elastic deformation and rupture. Based on the Taylor expansion strategy, SCABBIA *et al.* [14, 15] put forward a technique to impose boundary conditions in ordinary state-based peridynamics. A Peridynamic Galerkin method allowing direct imposition of boundary conditions was also proposed in [43] based on the weak form of PD. In [44], a technique directly imposing boundary conditions on the outer layer was introduced by the peridynamic differential operator (PDDO) [44].

Although an endeavor has been undertaken to find the analytic solution of PD, for example, SILLING *et al.* studied the deformation of bar [3], WECKNER *et al.* obtained the integral expression of the three-dimensional PD solution [16], and Mikata studied the analytical solutions of peristatic of a 1D infinite rod [17], it is very difficult to analytically solve the system of integro-differential equations. Therefore, a common treatment tends to be numerical computation, but this makes dealing with boundary conditions trickier. To find the numerical solution of PD, it is necessary to select the suitable spatial discrete and temporal

discrete scheme. The spatial discrete scheme can be adopted by either the mesh-free method or the finite element method. The temporal discrete scheme can be roughly divided into explicit and implicit formats, although the mixed explicit-implicit time integration scheme has been proposed in literature [18]. In the explicit scheme, the results of the next time step can be directly given by the data of the current time step, such as the central difference scheme. In the implicit scheme, the results of the next time step need to be acquired by iteration, and it usually causes the large-matrix operations, such as the Newton–Raphson scheme. In the early days, the meshfree spatial discrete scheme was usually matched with the temporal explicit scheme. For example, SILLING [4, 19] firstly used this method to solve PD dynamic problems. Sequentially, the adaptive dynamic relaxation method (ADR) [20] was applied to solve PD quasi-static problems while the explicit integration scheme was also employed to simulate high-velocity impact fracturing in [21]. Owing to the similarity between the discrete PD scheme and molecular dynamics, the molecular dynamics package LAMMPS [22] can be directly used to solve the PD problems. The implicit scheme was also used to match the meshfree spatial discrete scheme. Mitchel used an implicit method to solve dynamic and quasi-static problems based on the ordinary state-based plasticity [23] and viscoelasticity model [24]. The implicit method can be also used to solve quasi-static problems of the non-ordinary state-based with finite deformation in [25]. LOPEZ [26] utilized Newmark- β method in PD simulation.

When the finite element method is adopted for spatial discretization, the stiffness matrix assembly method of the finite element can be used in the implicit scheme. GERSTLE [27] performed the PD simulation for concrete structures using the finite element discretization. GUNZBURGER [28] proposed discontinuous Galerkin methods to solve PD discontinuity problems. For many local and non-local coupled models, the spatial discretization based on the finite element method is widely used in the explicit or implicit scheme. Some examples can be found in SILLING [8], ZINGALES [29] and HAN *et al.* [30–32].

In this paper, the concrete formulation of the peridynamic equation of motion with the boundary condition (PDBC) is determined by reducing the three undetermined scalar transfer functions [11] into a scalar generating function. In addition, we use MATLAB to implement a nonlinear implicit solver.

The outline of the paper is as follows. In Section 2, peridynamics compatible with boundary conditions is introduced. Section 3 is divided into four parts. Firstly, the balance equation of energy is proved to have the same form as that of original PD after the boundary conditions are introduced into the peridynamic equation of motion. This ensures that the constitutive equation of original PD can be directly inherited by PDBC. Then, the bond-based constitutive equation and the ordinary state-based constitutive equation are given, respectively. Finally, the transfer functions involved in PDBC are constructed. In Section 4,

the implicit numerical algorithm used to solve PDBC is presented. In Section 5, PDBC is used to calculate the benchmark problems of a rectangular plate under three types of boundary conditions and comparison with the classical elasticity theory and original PD is given. Finally, we close this paper with conclusions.

2. New peridynamic equation of motion

2.1. Peridynamic equation of motion with boundary conditions

In the peridynamic theory proposed by Silling, the equation of motion can be expressed by the following integro-differential form [2]:

$$(2.1) \quad \rho(\mathbf{x})\ddot{\mathbf{u}}(\mathbf{x}, t) = \int_{H_{\mathbf{x}}} \{ \mathbf{T}[\mathbf{x}, t] \langle \boldsymbol{\xi} \rangle - \mathbf{T}[\mathbf{x}', t] \langle -\boldsymbol{\xi} \rangle \} dV_{\mathbf{x}'} + \mathbf{b}(\mathbf{x}, t),$$

where $\boldsymbol{\xi} = \mathbf{x}' - \mathbf{x}$; H_x is a spherical neighborhood of \mathbf{x} with radius δ . In Eq. (2.1), the displacement field \mathbf{u} is of the Lagrangian form and the volume integral is over the initial configuration.

Equation (2.1) is inconsistent with the traction boundary condition. In order to offset this deficiency, a new peridynamic equation of motion is proposed in [11], which reads:

$$(2.2) \quad \rho(\mathbf{x})\ddot{\mathbf{u}}(\mathbf{x}, t) = \int_{\partial\Omega} \{ G(\mathbf{x}, \mathbf{x}''') \mathbf{p}(\mathbf{x}''', t) + L(\mathbf{x}, \mathbf{x}''') \mathbf{y}'''(\mathbf{x}''', t) \} dA_{\mathbf{x}'''} \\ + \int_{H_{\mathbf{x}}} \{ \mathbf{T}[\mathbf{x}, t] \langle \boldsymbol{\xi} \rangle - \mathbf{T}[\mathbf{x}', t] \langle -\boldsymbol{\xi} \rangle \} dV_{\mathbf{x}'} + \mathbf{b}(\mathbf{x}, t),$$

where $\partial\Omega$ denotes the surface of peridynamic media Ω in the initial configuration, \mathbf{x}''' is a position vector of a particle on $\partial\Omega$, $\mathbf{y}'''(\mathbf{x}''', t) = \mathbf{x}''' + \mathbf{u}'''(\mathbf{x}''', t)$ is the position vector of \mathbf{x}''' in the deformed configuration and is shortened to \mathbf{y}''' , that is, \mathbf{y}''' is the motion of $\partial\Omega$, and \mathbf{u}''' is a displacement field of the Lagrangian form; $\mathbf{p}(\mathbf{x}''', t)$ is the traction prescribed on $\partial\Omega$, $G(\mathbf{x}, \mathbf{x}''')$ with the dimension of $1/m^3$ and $L(\mathbf{x}, \mathbf{x}''')$ with the dimension of N/m^6 are the transfer function of the boundary traction and of the boundary displacement constraint, respectively. They transfer the effects of the traction and the displacement constraint into every particle within material.

It has been proved in [11] that Eq. (2.2) satisfies the conservation law of momentum and is a form-invariant under the Galileo transformation, when:

$$(2.3) \quad \int_{\Omega} G(\mathbf{x}, \mathbf{x}''') dV_{\mathbf{x}'''} = 1,$$

$$(2.4) \quad \int_{\Omega} L(\mathbf{x}, \mathbf{x}''') dV_{\mathbf{x}} = 0,$$

$$(2.5) \quad \int_{\partial\Omega} L(\mathbf{x}, \mathbf{x}''') dA_{\mathbf{x}'''} = 0.$$

In addition, it is also certified in [11] that in order to make Eq. (2.2) compatible with the conservation law of angular momentum, $\mathbf{p}(\mathbf{x}''', t)$, $\mathbf{y}'''(\mathbf{x}''', t)$, $\mathbf{y}(\mathbf{x}, t)$ must satisfy the constraints below

$$(2.6) \quad J(\mathbf{x}, \mathbf{x}''')[\mathbf{y}'''(\mathbf{x}''', t) - \mathbf{y}(\mathbf{x}, t)] = G(\mathbf{x}, \mathbf{x}''')\mathbf{p}(\mathbf{x}''', t) + L(\mathbf{x}, \mathbf{x}''')\mathbf{y}'''(\mathbf{x}''', t),$$

where $J(\mathbf{x}, \mathbf{x}''')$ is the boundary influence function and with the dimension of N/m^6 . In fact, Eq. (2.6) can be regarded as a constitutive equation with relevance to the traction and displacement constraints on the boundary surface. So $J(\mathbf{x}, \mathbf{x}''')$ is also a stiffness coefficient. It is worth noting that the existence of function $L(\mathbf{x}, \mathbf{x}''')$ ensures that Eq. (2.2) satisfies the equilibrium of angular momentum, so it cannot be zero.

When $\mathbf{x} = \mathbf{x}'''$, Eq. (2.6) reduces to

$$(2.7) \quad G(\mathbf{x}''', \mathbf{x}''')\mathbf{p}(\mathbf{x}''', t) + L(\mathbf{x}''', \mathbf{x}''')\mathbf{y}'''(\mathbf{x}''', t) = \mathbf{0}.$$

Since $\mathbf{y}'''(\mathbf{x}''', t)$ and $\mathbf{p}(\mathbf{x}''', t)$ are correlated with each other, the two equalities in [11], i.e.,

$$(2.8) \quad \begin{cases} G(\mathbf{x}''', \mathbf{x}''') = 0, \\ L(\mathbf{x}''', \mathbf{x}''') = 0 \end{cases}$$

are no longer considered to be valid. In other words, the constraints on $G(\mathbf{x}, \mathbf{x}''')$ and $L(\mathbf{x}, \mathbf{x}''')$ in [11] are relaxed in this paper.

Combining Eq. (2.6), the first term at the right end of Eq. (2.2) can be used to represent the displacement, traction or mixed boundary conditions. Firstly, if the displacement boundary condition $\mathbf{y}'''(\mathbf{x}''', t) = \bar{\mathbf{y}}(\mathbf{x}''', t) = \mathbf{x}''' + \bar{\mathbf{u}}(\mathbf{x}''', t)$ is given, then substituting Eq. (2.6) into Eq. (2.2) leads to

$$(2.9) \quad \rho(\mathbf{x})\ddot{\mathbf{u}}(\mathbf{x}, t) = \int_{\partial\Omega_u} J(\mathbf{x}, \mathbf{x}''')[\bar{\mathbf{y}}(\mathbf{x}''', t) - \mathbf{y}(\mathbf{x}, t)] dA_{\mathbf{x}'''} \\ + \int_{H_{\mathbf{x}}} \{\mathbf{T}[\mathbf{x}, t]\langle \boldsymbol{\xi} \rangle - \mathbf{T}[\mathbf{x}', t]\langle -\boldsymbol{\xi} \rangle\} dV_{\mathbf{x}'} + \mathbf{b}(\mathbf{x}, t),$$

which is the peridynamic equation of motion with the displacement boundary condition. In this case, $\partial\Omega_u = \partial\Omega$.

Then, if the traction boundary condition $\mathbf{p}(\mathbf{x}''', t) = \bar{\mathbf{p}}(\mathbf{x}''', t)$ is given, $\mathbf{y}'''(\mathbf{x}''', t)$ can be acquired by solving Eq. (2.6), that is

$$(2.10) \quad \mathbf{y}'''(\mathbf{x}''', t) = \frac{G(\mathbf{x}, \mathbf{x}''')}{J(\mathbf{x}, \mathbf{x}''') - L(\mathbf{x}, \mathbf{x}''')} \bar{\mathbf{p}}(\mathbf{x}''', t) + \frac{J(\mathbf{x}, \mathbf{x}''')}{J(\mathbf{x}, \mathbf{x}''') - L(\mathbf{x}, \mathbf{x}''')} \mathbf{y}(\mathbf{x}, t).$$

By substituting Eq. (2.10) into Eq. (2.2), the peridynamic equation of motion with the traction boundary condition is given as follows

$$(2.11) \quad \rho(\mathbf{x})\ddot{\mathbf{u}}(\mathbf{x}, t) = \int_{\partial\Omega_p} \{\alpha(\mathbf{x}, \mathbf{x}''')\bar{\mathbf{p}}(\mathbf{x}''', t) + \beta(\mathbf{x}, \mathbf{x}''')\mathbf{y}(\mathbf{x}, t)\} dA_{\mathbf{x}'''} \\ + \int_{H_{\mathbf{x}}} \{\underline{\mathbf{T}}[\mathbf{x}, t]\langle \boldsymbol{\xi} \rangle - \underline{\mathbf{T}}[\mathbf{x}', t]\langle -\boldsymbol{\xi} \rangle\} dV_{\mathbf{x}'} + \mathbf{b}(\mathbf{x}, t),$$

where $\partial\Omega_p = \partial\Omega$, and

$$(2.12) \quad \begin{cases} \alpha(\mathbf{x}, \mathbf{x}''') = \frac{J(\mathbf{x}, \mathbf{x}''')G(\mathbf{x}, \mathbf{x}''')}{J(\mathbf{x}, \mathbf{x}''') - L(\mathbf{x}, \mathbf{x}''')}, \\ \beta(\mathbf{x}, \mathbf{x}''') = \frac{J(\mathbf{x}, \mathbf{x}''')L(\mathbf{x}, \mathbf{x}''')}{J(\mathbf{x}, \mathbf{x}''') - L(\mathbf{x}, \mathbf{x}''')}. \end{cases}$$

Clearly, $J(\mathbf{x}, \mathbf{x}''')$ cannot be equal to $L(\mathbf{x}, \mathbf{x}''')$ to guarantee that Eq. (2.12) is non-singular.

Finally, let $\partial\Omega_u \cup \partial\Omega_p = \partial\Omega$ and $\partial\Omega_u \cap \partial\Omega_p = \emptyset$. Combining Eq. (2.9) with Eq. (2.11), we have

$$(2.13) \quad \rho(\mathbf{x})\ddot{\mathbf{u}}(\mathbf{x}, t) = \int_{\partial\Omega_u} J(\mathbf{x}, \mathbf{x}''')[\bar{\mathbf{y}}(\mathbf{x}''', t) - \mathbf{y}(\mathbf{x}, t)] dA_{\mathbf{x}'''} \\ + \int_{\partial\Omega_p} \{\alpha(\mathbf{x}, \mathbf{x}''')\bar{\mathbf{p}}(\mathbf{x}''', t) + \beta(\mathbf{x}, \mathbf{x}''')\mathbf{y}(\mathbf{x}, t)\} dA_{\mathbf{x}'''} \\ + \int_{H_{\mathbf{x}}} \{\underline{\mathbf{T}}[\mathbf{x}, t]\langle \boldsymbol{\xi} \rangle - \underline{\mathbf{T}}[\mathbf{x}', t]\langle -\boldsymbol{\xi} \rangle\} dV_{\mathbf{x}'} + \mathbf{b}(\mathbf{x}, t).$$

As a result, we acquire the peridynamic equation of motion with the mixed boundary condition. Clearly, $\alpha(\mathbf{x}, \mathbf{x}''')$ and $\beta(\mathbf{x}, \mathbf{x}''')$ has the dimension of $1/\text{m}^3$ and N/m^6 , respectively.

2.2. Simplification of the peridynamic equation of motion with boundary conditions

From Eq. (2.6), it can be seen that $J(\mathbf{x}, \mathbf{x}''')$ and $L(\mathbf{x}, \mathbf{x}''')$ have the same dimension, hence, we set

$$(2.14) \quad J(\mathbf{x}, \mathbf{x}''') = \chi L(\mathbf{x}, \mathbf{x}'''),$$

where χ is a dimensionless constant, and it cannot be equal to 1 and 0. Equations (2.14), (2.9), (2.11) and Eq. (2.13) lead to

$$(2.15) \quad \rho(\mathbf{x})\ddot{\mathbf{u}}(\mathbf{x}, t) = \chi \int_{\partial\Omega_u} L(\mathbf{x}, \mathbf{x}''') [\bar{\mathbf{y}}(\mathbf{x}''', t) - \mathbf{y}(\mathbf{x}, t)] dA_{\mathbf{x}'''} \\ + \int_{H_{\mathbf{x}}} \{ \underline{\mathbf{T}}[\mathbf{x}, t] \langle \boldsymbol{\xi} \rangle - \underline{\mathbf{T}}[\mathbf{x}', t] \langle -\boldsymbol{\xi} \rangle \} dV_{\mathbf{x}'} + \mathbf{b}(\mathbf{x}, t),$$

where $\partial\Omega_u = \partial\Omega$,

$$(2.16) \quad \rho(\mathbf{x})\ddot{\mathbf{u}}(\mathbf{x}, t) = \frac{\chi}{\chi - 1} \int_{\partial\Omega_p} \{ G(\mathbf{x}, \mathbf{x}''') \bar{\mathbf{p}}(\mathbf{x}''', t) + L(\mathbf{x}, \mathbf{x}''') \mathbf{y}(\mathbf{x}, t) \} dA_{\mathbf{x}'''} \\ + \int_{H_{\mathbf{x}}} \{ \underline{\mathbf{T}}[\mathbf{x}, t] \langle \boldsymbol{\xi} \rangle - \underline{\mathbf{T}}[\mathbf{x}', t] \langle -\boldsymbol{\xi} \rangle \} dV_{\mathbf{x}'} + \mathbf{b}(\mathbf{x}, t),$$

where $\partial\Omega_p = \partial\Omega$,

$$(2.17) \quad \rho(\mathbf{x})\ddot{\mathbf{u}}(\mathbf{x}, t) = \chi \int_{\partial\Omega_u} L(\mathbf{x}, \mathbf{x}''') [\bar{\mathbf{y}}(\mathbf{x}''', t) - \mathbf{y}(\mathbf{x}, t)] dA_{\mathbf{x}'''} \\ + \frac{\chi}{\chi - 1} \int_{\partial\Omega_p} \{ G(\mathbf{x}, \mathbf{x}''') \bar{\mathbf{p}}(\mathbf{x}''', t) + L(\mathbf{x}, \mathbf{x}''') \mathbf{y}(\mathbf{x}, t) \} dA_{\mathbf{x}'''} \\ + \int_{H_{\mathbf{x}}} \{ \underline{\mathbf{T}}[\mathbf{x}, t] \langle \boldsymbol{\xi} \rangle - \underline{\mathbf{T}}[\mathbf{x}', t] \langle -\boldsymbol{\xi} \rangle \} dV_{\mathbf{x}'} + \mathbf{b}(\mathbf{x}, t),$$

where $\partial\Omega_u \cup \partial\Omega_p = \partial\Omega$ and $\partial\Omega_u \cap \partial\Omega_p = \emptyset$.

Because of the constraint of Eq. (2.5), Eq. (2.15) and Eq. (2.16) further reduce to:

$$(2.18) \quad \rho(\mathbf{x})\ddot{\mathbf{u}}(\mathbf{x}, t) = \chi \int_{\partial\Omega_u} L(\mathbf{x}, \mathbf{x}''') \bar{\mathbf{y}}(\mathbf{x}''', t) dA_{\mathbf{x}'''} \\ + \int_{H_{\mathbf{x}}} \{ \underline{\mathbf{T}}[\mathbf{x}, t] \langle \boldsymbol{\xi} \rangle - \underline{\mathbf{T}}[\mathbf{x}', t] \langle -\boldsymbol{\xi} \rangle \} dV_{\mathbf{x}'} + \mathbf{b}(\mathbf{x}, t),$$

$$(2.19) \quad \rho(\mathbf{x})\ddot{\mathbf{u}}(\mathbf{x}, t) = \frac{\chi}{\chi - 1} \int_{\partial\Omega_p} G(\mathbf{x}, \mathbf{x}''') \bar{\mathbf{p}}(\mathbf{x}''', t) dA_{\mathbf{x}'''} \\ + \int_{H_{\mathbf{x}}} \{ \underline{\mathbf{T}}[\mathbf{x}, t] \langle \boldsymbol{\xi} \rangle - \underline{\mathbf{T}}[\mathbf{x}', t] \langle -\boldsymbol{\xi} \rangle \} dV_{\mathbf{x}'} + \mathbf{b}(\mathbf{x}, t).$$

Equations (2.17), (2.18) and Eq. (2.19) are called PDBC.

3. Peridynamic constitutive models of elastic deformation and transfer functions

3.1. Balance equation of energy

Let $\mathbf{v} = \mathbf{v}(\mathbf{x})$ is the velocity field within material, and ε is internal energy of per unit mass. Only elastic deformation is concerned, in peridynamics with boundary traction, total energy equilibrium [33] can be represented as

$$(3.1) \quad \frac{D}{Dt} \int_{\Omega} \left(\frac{1}{2} \rho \mathbf{v}^2 + \rho \varepsilon \right) dV \\ = \int_{\Omega} \left\{ \int_{\partial\Omega} [G(\mathbf{x}, \mathbf{x}''') \mathbf{p}(\mathbf{x}''', t) + L(\mathbf{x}, \mathbf{x}''') \mathbf{y}'''(\mathbf{x}'', t)] dA_{\mathbf{x}'''} \right\} \cdot \mathbf{v} dV_{\mathbf{x}} + \int_{\Omega} \mathbf{b} \cdot \mathbf{v} dV.$$

Equation (3.1) can be further written as

$$(3.2) \quad \int_{\Omega} \rho \ddot{\mathbf{u}} \cdot \mathbf{v} dV + \int_{\Omega} \rho \dot{\varepsilon} dV \\ = \int_{\Omega} \left\{ \int_{\partial\Omega} [G(\mathbf{x}, \mathbf{x}''') \mathbf{p}(\mathbf{x}''', t) + L(\mathbf{x}, \mathbf{x}''') \mathbf{y}'''(\mathbf{x}''', t)] dA_{\mathbf{x}'''} \right\} \cdot \mathbf{v} dV_{\mathbf{x}} + \int_{\Omega} \mathbf{b} \cdot \mathbf{v} dV.$$

In terms of Eq. (2.2), Eq. (3.2) can reduce to

$$(3.3) \quad \int_{\Omega} \rho \dot{\varepsilon} dV = \int_{\Omega} \left\{ \int_{H_{\mathbf{x}}} \{ \underline{\mathbf{T}}[\mathbf{x}', t] \langle -\boldsymbol{\xi} \rangle - \underline{\mathbf{T}}[\mathbf{x}, t] \langle \boldsymbol{\xi} \rangle \} dV_{\mathbf{x}'} \right\} \cdot \mathbf{v} dV_{\mathbf{x}}.$$

Since $H_x \subset \Omega$ is a compact supported set of $\underline{\mathbf{T}}[\mathbf{x}', t] \langle -\boldsymbol{\xi} \rangle$ and $\underline{\mathbf{T}}[\mathbf{x}, t] \langle \boldsymbol{\xi} \rangle$, Eq. (3.3) can be written as

$$(3.4) \quad \int_{\Omega} \rho \dot{\varepsilon} dV = \int_{\Omega} \left\{ \int_{\Omega} \{ \underline{\mathbf{T}}[\mathbf{x}', t] \langle -\boldsymbol{\xi} \rangle - \underline{\mathbf{T}}[\mathbf{x}, t] \langle \boldsymbol{\xi} \rangle \} dV_{\mathbf{x}'} \right\} \cdot \mathbf{v} dV_{\mathbf{x}}.$$

Interchanging \mathbf{x}' and \mathbf{x} , and then using a definition of the compact supported set, we have

$$(3.5) \quad \int_{\Omega} \rho \dot{\varepsilon} dV = \int_{\Omega} \left\{ \int_{H_{\mathbf{x}}} \underline{\mathbf{T}}[\mathbf{x}, t] \langle \boldsymbol{\xi} \rangle \cdot [\mathbf{v}(\mathbf{x}') - \mathbf{v}(\mathbf{x})] dV_{\mathbf{x}'} \right\} dV_{\mathbf{x}}.$$

Localization leads to the local statement of the balance equation of energy as follows

$$(3.6) \quad \rho \dot{\varepsilon} = \int_{H_{\mathbf{x}}} \underline{\mathbf{T}}[\mathbf{x}, t] \langle \boldsymbol{\xi} \rangle \cdot [\mathbf{v}(\mathbf{x}') - \mathbf{v}(\mathbf{x})] dV_{\mathbf{x}'},$$

which has the same form as that in peridynamics without boundary conditions [33], and it is a base to determine the peridynamic constitutive models of hyperelastic material. Therefore, hyperelastic constitutive models in peridynamics without boundary conditions can be inherited without modification by peridynamics with boundary conditions.

3.2. Bond-based constitutive model

The bond-based (BB) constitutive models have been established by SILLING [1]. They characterize the spring-like interactions between the material point \mathbf{x} and \mathbf{x}' . A typical BB constitutive model is the prototype microelastic (PM) model, which reads [4, 34]

$$(3.7) \quad \mathbf{f}(\mathbf{y}, \mathbf{y}') = \begin{cases} C(\mathbf{x}, \mathbf{x}')e\mathbf{M} = \frac{c}{|\boldsymbol{\xi}|}e\mathbf{M} = cs\mathbf{M} = c\frac{|\mathbf{y}' - \mathbf{y}| - |\boldsymbol{\xi}|}{|\boldsymbol{\xi}|}\frac{\mathbf{y}' - \mathbf{y}}{|\mathbf{y}' - \mathbf{y}|}, & |\boldsymbol{\xi}| \leq \delta, \\ \mathbf{0} & \text{otherwise,} \end{cases}$$

where $\mathbf{f}(\mathbf{y}, \mathbf{y}')$ is the force density vector [1], $C(\mathbf{x}, \mathbf{x}')$ the so-called micromodulus, c called the spring constant or the bond-constant, $e = |\mathbf{y}' - \mathbf{y}| - |\boldsymbol{\xi}|$ the bond extension, $s = (|\mathbf{y}' - \mathbf{y}| - |\boldsymbol{\xi}|)/|\boldsymbol{\xi}|$ called the bond stretch or the bond strain, and \mathbf{M} a unit vector in the direction of the deformed bond from \mathbf{x} to \mathbf{x}' .

In the PM model, the only peridynamic model parameter c can be calibrated through equivalence of the strain energy density. After calibration, it can be written as [34]

$$(3.8) \quad c = \begin{cases} \frac{12E}{\pi\delta^4} & \text{3-dimension,} \\ \frac{9E}{\pi h\delta^3} & \text{2-dimension plane stress,} \\ \frac{48E}{5\pi h\delta^3} & \text{2-dimension plane strain,} \\ \frac{2E}{h_1\delta^2} & \text{1-dimension,} \end{cases}$$

where E is the Young modulus, h is the plate thickness, and h_1 is the cross-sectional area of the plate. PM model treats each bond as a linear elastic spring. Therefore, the bulk material properties are also elastic.

The distinguishing feature of BB models is that each bond force density $\mathbf{f}(\mathbf{y}, \mathbf{y}')$ depends only on $\mathbf{y}' - \mathbf{y}$. Consequently, in BB models, the Poisson ratio of 3D and 2D plane strain problems are fixed at 1/4, while that of 2D plane stress problem are fixed at 1/3.

3.3. Ordinary state-based constitutive model

The state-based (SB) constitutive models are established firstly by SILLING [2]. SB models associate a force state at \mathbf{x} with the collective deformation of the entire family of \mathbf{x} , in which the restriction of Poisson's ratio is relaxed to some extent. SB models contains the ordinary state-based (OSB) models and the non-ordinary state-based (NOSB) models. In the OSB models, the bond force density vector $\underline{\mathbf{T}}\langle\xi\rangle$ is always parallel to the deformed bond $\underline{\mathbf{Y}}\langle\xi\rangle$, namely $\underline{\mathbf{T}} = \underline{t}\underline{\mathbf{M}}$ [2], where ξ is any bond in the family; $\underline{\mathbf{T}}$ is a force vector state field; $\underline{\mathbf{Y}}$ is a deformation vector state field; \underline{t} is a force scalar state field; $\underline{\mathbf{M}}$ is the deformed direction vector state field (in BB models, $\underline{\mathbf{M}}$ denoted \mathbf{M}).

A reformulated OSB model for isotropic elastic material expounded by MADENCI and OTERKUS is written as [35, 36]

$$(3.9) \quad \underline{\mathbf{T}}[\mathbf{x}, t]\langle\xi\rangle - \underline{\mathbf{T}}[\mathbf{x}', t]\langle-\xi\rangle = \begin{cases} \frac{1}{2}(\underline{A} + \underline{B})\underline{\mathbf{M}}, & |\xi| \leq \delta, \\ \mathbf{0} & \text{otherwise,} \end{cases}$$

where \underline{A} and \underline{B} both are two force scalar state, which read

$$(3.10) \quad \begin{cases} \underline{A} = 4\omega\langle|\mathbf{x}' - \mathbf{x}|\rangle \left[d \left(\frac{\mathbf{y}' - \mathbf{y}}{|\mathbf{y}' - \mathbf{y}|} \cdot \frac{\mathbf{x}' - \mathbf{x}}{|\mathbf{x}' - \mathbf{x}|} \right) (a\theta_{\mathbf{x}}) + b\underline{e} \right] \\ \quad = \frac{4\delta}{|\mathbf{x}' - \mathbf{x}|} \left[d \left(\frac{\mathbf{y}' - \mathbf{y}}{|\mathbf{y}' - \mathbf{y}|} \cdot \frac{\mathbf{x}' - \mathbf{x}}{|\mathbf{x}' - \mathbf{x}|} \right) (a\theta_{\mathbf{x}}) + b(|\mathbf{y}' - \mathbf{y}| - |\xi|) \right], \\ \underline{B} = 4\omega\langle|\mathbf{x}' - \mathbf{x}|\rangle \left[d \left(\frac{\mathbf{y} - \mathbf{y}'}{|\mathbf{y} - \mathbf{y}'|} \cdot \frac{\mathbf{x} - \mathbf{x}'}{|\mathbf{x} - \mathbf{x}'|} \right) (a\theta_{\mathbf{x}'}) + b\underline{e} \right] \\ \quad = \frac{4\delta}{|\mathbf{x} - \mathbf{x}'|} \left[d \left(\frac{\mathbf{y} - \mathbf{y}'}{|\mathbf{y} - \mathbf{y}'|} \cdot \frac{\mathbf{x} - \mathbf{x}'}{|\mathbf{x} - \mathbf{x}'|} \right) (a\theta_{\mathbf{x}'}) + b(|\mathbf{y} - \mathbf{y}'| - |\xi|) \right]. \end{cases}$$

In Eq. (3.10), $\omega = \delta/|\xi|$ is a spherical influence function [2] and $\underline{e} = |\mathbf{y}' - \mathbf{y}| - |\xi|$ is a scalar state describing deformation. θ_x and $\theta_{x'}$ are the dilatations at the point \mathbf{x} and \mathbf{x}' , respectively. They can be represented as

$$(3.11) \quad \begin{cases} \theta_{\mathbf{x}} = d \int_{H_{\mathbf{x}}} \left[\omega\langle|\mathbf{x}' - \mathbf{x}|\rangle \frac{|\mathbf{y}' - \mathbf{y}| - |\mathbf{x}' - \mathbf{x}|}{|\mathbf{x}' - \mathbf{x}|} \frac{\mathbf{y}' - \mathbf{y}}{|\mathbf{y}' - \mathbf{y}|} (\mathbf{x}' - \mathbf{x}) \right] dv_{\mathbf{x}} \\ \quad = d \int_{H_{\mathbf{x}}} \left[\frac{\delta}{|\mathbf{x}' - \mathbf{x}|} \frac{|\mathbf{y}' - \mathbf{y}| - |\mathbf{x}' - \mathbf{x}|}{|\mathbf{x}' - \mathbf{x}|} \frac{\mathbf{y}' - \mathbf{y}}{|\mathbf{y}' - \mathbf{y}|} (\mathbf{x}' - \mathbf{x}) \right] dv_{\mathbf{x}}, \\ \theta_{\mathbf{x}'} = d \int_{H_{\mathbf{x}'}} \left[\omega\langle|\mathbf{x}'' - \mathbf{x}'|\rangle \frac{|\mathbf{y}'' - \mathbf{y}'| - |\mathbf{x}'' - \mathbf{x}'|}{|\mathbf{x}'' - \mathbf{x}'|} \frac{\mathbf{y}'' - \mathbf{y}'}{|\mathbf{y}'' - \mathbf{y}'|} (\mathbf{x}'' - \mathbf{x}') \right] dv_{\mathbf{x}'} \\ \quad = d \int_{H_{\mathbf{x}'}} \left[\frac{\delta}{|\mathbf{x}'' - \mathbf{x}'|} \frac{|\mathbf{y}'' - \mathbf{y}'| - |\mathbf{x}'' - \mathbf{x}'|}{|\mathbf{x}'' - \mathbf{x}'|} \frac{\mathbf{y}'' - \mathbf{y}'}{|\mathbf{y}'' - \mathbf{y}'|} (\mathbf{x}'' - \mathbf{x}') \right] dv_{\mathbf{x}'}. \end{cases}$$

Here \mathbf{x}'' represents the position vector of a particle in the neighborhood of \mathbf{x}' in the initial configuration while \mathbf{y}'' is the position vector of \mathbf{x}'' in the deformed configuration.

The OSB model above has three peridynamic model parameters, namely d , a and b . In terms of equivalence of strain energy density, these parameters are determined by [35, 36]:

$$(3.12) \quad d = \begin{cases} \frac{9}{4\pi\delta^4} & \text{3-dimension,} \\ \frac{2}{\pi h\delta^3} & \text{2-dimension plane stress,} \\ \frac{1}{2h_1\delta^2} & \text{1-dimension,} \end{cases}$$

$$(3.13) \quad a = \begin{cases} \frac{E(11\nu - 4)}{6(1 - 2\nu)(1 + \nu)} & \text{3-dimension,} \\ \frac{E(3\nu - 1)}{4(1 - \nu)(1 + \nu)} & \text{2-dimension plane stress,} \\ 0 & \text{1-dimension,} \end{cases}$$

$$(3.14) \quad b = \begin{cases} \frac{15E}{4(1 + \nu)\pi\delta^5} & \text{3-dimension,} \\ \frac{3E}{(1 + \nu)\pi h\delta^4} & \text{2-dimension plane stress,} \\ \frac{E}{2h_1\delta^3} & \text{1-dimension,} \end{cases}$$

where ν is the Poisson ratio.

It can be seen from Eq. (3.14) that parameter b and parameter c satisfy $c = 4b\delta$. Consequently, when $ad = 0$, the OSB model reformulated by MADENCI [35, 36] is equivalent to the PM model. In addition, it should be noted that $\underline{\mathbf{T}}[\mathbf{x}, t]\langle \xi \rangle$ and $\underline{\mathbf{T}}[\mathbf{x}', t]\langle -\xi \rangle$ are not the acting and reacting forces, although they are in opposite directions, they are not equal in magnitude.

3.4. Construction of the transfer functions

The transfer functions contain the transfer function of the boundary displacement constraint $L(\mathbf{x}, \mathbf{x}''')$ and the transfer function of the boundary traction $G(\mathbf{x}, \mathbf{x}''')$. Although there is no unique construction way, in order to reduce computational cost, as few undetermined functions as possible should be introduced to represent $L(\mathbf{x}, \mathbf{x}''')$ and $G(\mathbf{x}, \mathbf{x}''')$. For this, we choose an integrable function $q(|\mathbf{x} - \mathbf{x}'''|)$ of two variables to form $L(\mathbf{x}, \mathbf{x}''')$ and $G(\mathbf{x}, \mathbf{x}''')$ as follows:

$$(3.15) \quad L(\mathbf{x}, \mathbf{x}''') = \lambda \left\{ q(|\mathbf{x} - \mathbf{x}'''|) \left[\int_{\partial\Omega} \int_{\Omega} q(|\mathbf{x} - \mathbf{x}'''|) dV_{\mathbf{x}} dA_{\mathbf{x}'''} \right] - \left[\int_{\partial\Omega} q(|\mathbf{x} - \mathbf{x}'''|) dA_{\mathbf{x}'''} \right] \left[\int_{\Omega} q(|\mathbf{x} - \mathbf{x}'''|) dV_{\mathbf{x}} \right] \right\},$$

$$(3.16) \quad G(\mathbf{x}, \mathbf{x}''') = \frac{q(|\mathbf{x} - \mathbf{x}'''|)}{\int_{\Omega} q(|\mathbf{x} - \mathbf{x}'''|) dV_{\mathbf{x}}},$$

where $q(|\mathbf{x} - \mathbf{x}'''|)$ is called the generating function of the transfer functions, which is dimensionless due to the following Eq. (3.17). In Eq. (3.15), the introduction of λ is to balance the dimensions on both sides of the equation, so its value is taken as 1 and the dimension is N/m^{11} . Clearly, $L(\mathbf{x}, \mathbf{x}''')$ and $G(\mathbf{x}, \mathbf{x}''')$ given by Eq. (3.15) and Eq. (3.16) satisfy the constraints of Eqs. (2.3)–(2.5). To avoid singularity, we set

$$(3.17) \quad q(|\mathbf{x} - \mathbf{x}'''|) = \begin{cases} \frac{\delta}{|\mathbf{x} - \mathbf{x}'''| + \delta} & |\mathbf{x} - \mathbf{x}'''| \leq \delta, \\ 0 & \text{otherwise.} \end{cases}$$

It is not difficult to find that $q(|\mathbf{x} - \mathbf{x}'''|)$ in (3.17) is dimensionless, and it makes the influences of the traction and displacement specified on the boundary surface confined to the boundary layer with the thickness of δ . Different from q proposed in [12], Eq. (3.17) has a similar form to the influence function in the constitutive model Eq. (3.10).

Physically, the effects caused by the prescribed displacement or traction at \mathbf{x}''' on the boundary surface can be always transmitted to a point \mathbf{x} in the interior of body through a path, even though there is a crack or void between the link between \mathbf{x}''' and \mathbf{x} . Similar to the influence functions in the peridynamic constitutive equations, the generating function Eq. (3.17) depends only on the distance between \mathbf{x}''' and \mathbf{x} , and attenuates with the increase of the distance.

4. Numerical algorithm for quasi-static problems

Since there are no large-matrix operations in the explicit solvers, the explicit solvers based on different schemes, such as the second-order central difference or the fourth-order Runge–Kutta scheme [18, 35, 37], have been developed and applied in numerous PD simulations. However, the explicit algorithm is conditionally convergent and stable, and artificial damping coefficients are introduced in the quasi-static analysis. Compared with the explicit algorithm, the implicit algorithm has higher accuracy and stability. Thus, we construct a nonlinear implicit algorithm based on the Newton–Raphson scheme [34, 38, 39].

The meshfree spatial discrete method [4] is used to discretize continuum into a range of arbitrary shaped subdomains. A collocation point, namely a node, is set at the centroid of each subdomain. As a result, the spatial discrete form of the quasi-static case of Eq. (2.17), Eq. (2.18) and Eq. (2.19) is written as:

$$(4.1) \quad \chi \sum_{\partial\Omega_u} L(\mathbf{x}_i, \mathbf{x}_k) [\bar{\mathbf{y}}(\mathbf{x}_k, t) - \mathbf{y}(\mathbf{x}_i, t)] A_{\mathbf{x}_k} \\ + \frac{\chi}{\chi - 1} \sum_{\partial\Omega_p} \{G(\mathbf{x}_i, \mathbf{x}_k) \bar{p}(\mathbf{x}_k, t) + L(\mathbf{x}_i, \mathbf{x}_k) \mathbf{y}(\mathbf{x}_i, t)\} A_{\mathbf{x}_k} \\ + \sum_{H_{\mathbf{x}_i}} \left\{ \mathbf{T}[\mathbf{x}_i, t] \langle \mathbf{x}_j - \mathbf{x}_i \rangle - \text{unT}[\mathbf{x}_j, t] \langle \mathbf{x}_i - \mathbf{x}_j \rangle \right\} V_{\mathbf{x}_j} + \mathbf{b}(\mathbf{x}_i, t) = \mathbf{0},$$

$$(4.2) \quad \chi \sum_{\partial\Omega_u} L(\mathbf{x}_i, \mathbf{x}_k) \bar{y}(\mathbf{x}_k, t) A_{\mathbf{x}_k} \\ + \sum_{H_{\mathbf{x}_i}} \left\{ \mathbf{T}[\mathbf{x}_i, t] \langle \mathbf{x}_j - \mathbf{x}_i \rangle - \mathbf{T}[\mathbf{x}_j, t] \langle \mathbf{x}_i - \mathbf{x}_j \rangle \right\} V_{\mathbf{x}_j} + \mathbf{b}(\mathbf{x}_i, t) = \mathbf{0},$$

$$(4.3) \quad \frac{\chi}{\chi - 1} \sum_{\partial\Omega_p} G(\mathbf{x}_i, \mathbf{x}_k) \bar{p}(\mathbf{x}_k, t) A_{\mathbf{x}_k} \\ + \sum_{H_{\mathbf{x}_i}} \left\{ \mathbf{T}[\mathbf{x}_i, t] \langle \mathbf{x}_j - \mathbf{x}_i \rangle - \mathbf{T}[\mathbf{x}_j, t] \langle \mathbf{x}_i - \mathbf{x}_j \rangle \right\} V_{\mathbf{x}_j} + \mathbf{b}(\mathbf{x}_i, t) = \mathbf{0}.$$

The same spatial discrete strategy can be applied to acquire the integral value of $L(\mathbf{x}, \mathbf{x}''')$ and $G(\mathbf{x}, \mathbf{x}''')$. When a constitutive model is nonlinear function of the displacement, the Newton–Raphson method will be used to obtain the numerical solution of the displacement. The details of the numerical algorithm refer to Appendix B.

5. Five benchmark problems in the plane elastic deformation

In this section, the plane benchmark problems of isotropic elastic rectangular plates are simulated. The geometric size and material properties of the plate are the same in the simulations and they are listed in Table 1. In addition, all length units are in millimeters [mm].

TABLE 1. Geometric and material parameters.

Length l [mm]	Width w [mm]	Young's modulus E [GPa]	Poisson's ratio ν
1000	500	200	0.3

The model parameter χ introduced in PDBC takes 3.59, which is given by an equivalent assumption that elastic solutions for the displacements at the ends

of a stretching rod are equal to the PD solutions. The detailed derivation refers to Appendix C.

5.1. Example 1: a rectangular plate with two opposite edges subjected to compression and the other two edges to the constraint of displacement

As shown in Fig. 1, two opposite edges of the rectangular plate are subjected to uniform compression $q = 180$ MPa, while other two edges are given the displacement $V_0 = 0.25$ mm in the y direction. Clearly, this is a mixed boundary value problem, corresponding to Eq. (2.17) or Eq. (4.1).

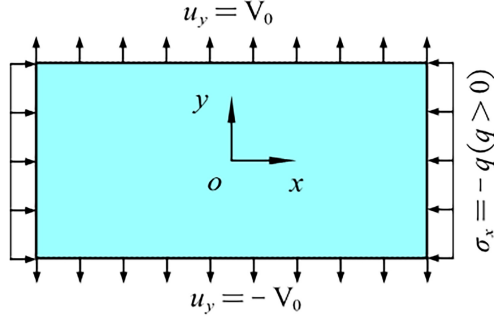


FIG. 1. Schematic diagram of subjected load of Example 1.

For simplicity, the rectangular plate is uniformly discretized into a particle set with the equal spacing Δ in the plane, as shown in Fig. 2. In calculation, the PM and OSB constitutive models are adopted.

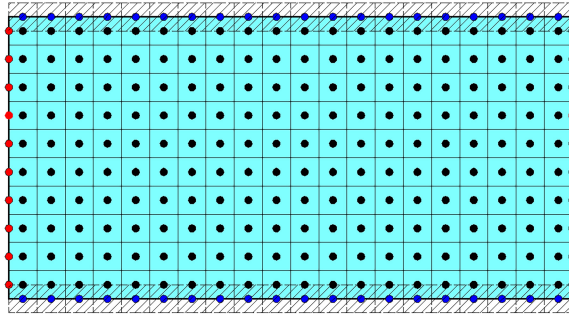


FIG. 2. Schematic diagram of the spatial discretization of the rectangular plate in Example 1.

In Fig. 2, the black dots represent the nodes within the plate, while the red and blue dots represent the nodes at the edges of the plate. As mentioned above, the blue dots are subjected to the constraint of a given displacement in the y direction and the red dots to the traction in the x direction. Since

the displacements of the blue dots in the x direction are still unknown, so the volume V_{xj} associated with these dots in Eq. (4.1) and Eq. (4.2) should be taken as $(\Delta^2 h)$ (see the shaded part in Fig. 2). It should be emphasized that embedding the fictitious volume $(\Delta^2 h)$ into the nodes on the displacement boundary is only a numerical processing means, which should be treated in all examples involving displacement boundary conditions.

The horizon size is specified as $\delta = 3.015\Delta$. The adaptive dynamic relaxation (ADR) method [20] is used to calculate PDBC, and three different grid sizes $\Delta = l/50$, $l/100$ and $l/200$ are used to show the influence of the grid density on the convergence and computational accuracy of the numerical algorithm, as illustrated in Figs. 3 to 8.

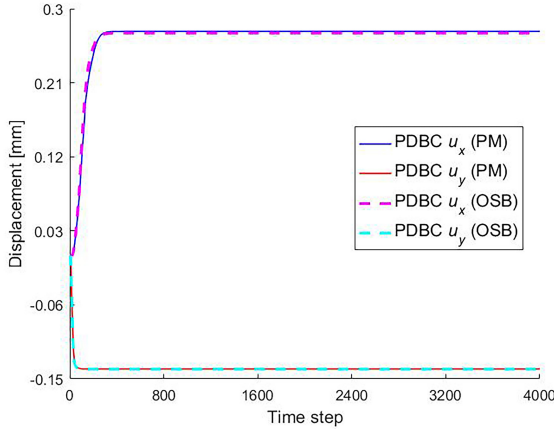


FIG. 3. Convergence of numerical algorithm at $x = -250$ mm and $y = -140$ mm with time step when $\Delta = l/50$.

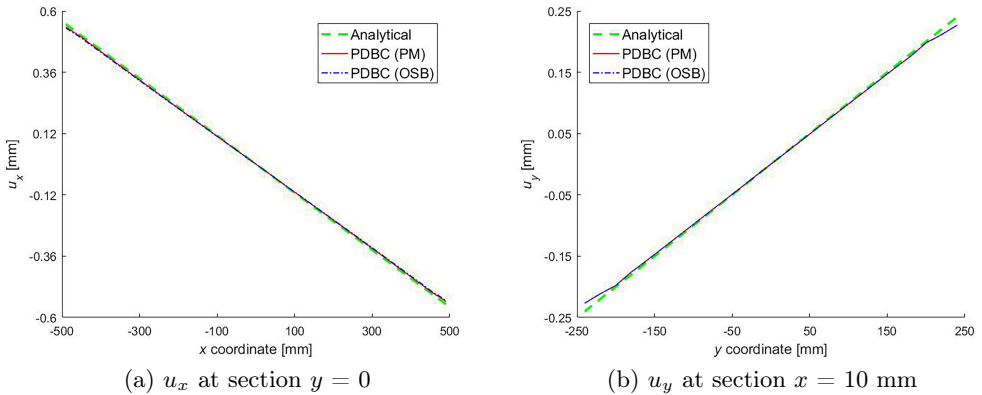


FIG. 4. The displacement at sections $y = 0$ and $x = 10$ mm when $\Delta = l/50$.

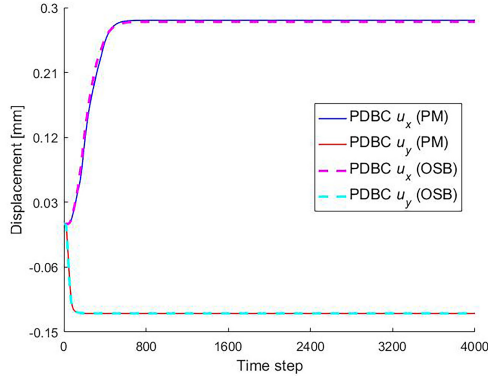


FIG. 5. Convergence of numerical algorithm at $x = -255$ mm and $y = -125$ mm with time step when $\Delta = l/100$.

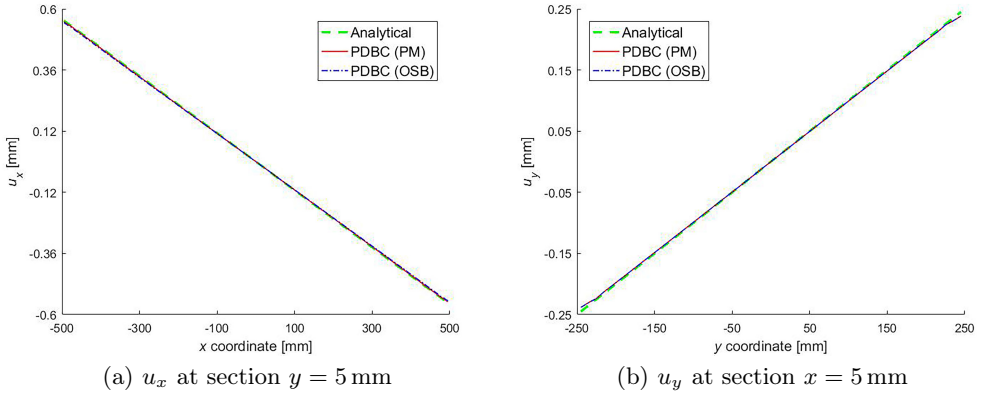


FIG. 6. The displacement at sections $y = 5$ mm and $x = 5$ mm when $\Delta = l/100$.

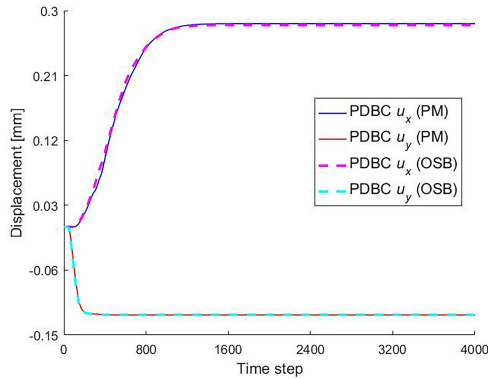


FIG. 7. Convergence of numerical algorithm at $x = -252.5$ mm and $y = -122.5$ mm with time step when $\Delta = l/200$.

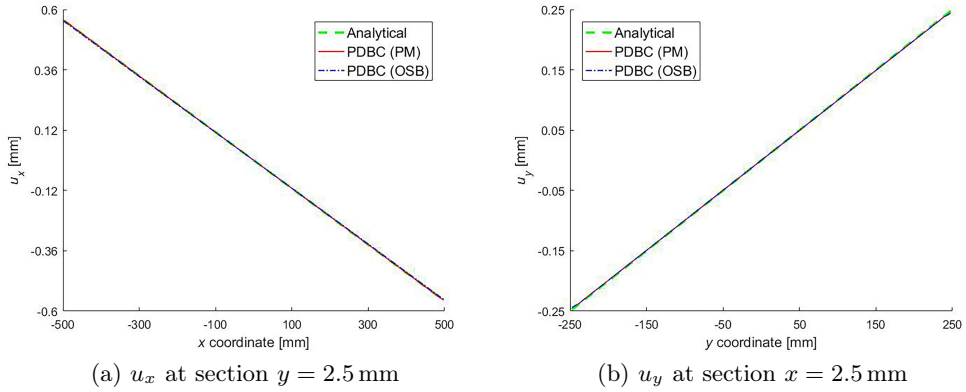


FIG. 8. The displacement at sections $y = 2.5$ mm and $x = 2.5$ mm when $\Delta = l/200$.

As can be seen from Figs. 3 to 8, as the grid density increases, the convergence rate of the numerical algorithm slows down, and the predicted results of PDBC are in good agreement with the classical solutions. Therefore, the δ -convergence [40] can be considered to satisfy for PDBC. In order to balance computational accuracy and efficiency, the grid size is taken as $\Delta = l/100$ by default in the subsequent simulation unless otherwise specified.

Figures 9 and 10 show that the numerical results obtained by the implicit solver implemented in this paper are remarkably in agreement with that by the ADR method. In the following, all simulations are based on the implicit solver.

From Figs. 11 and 12, it is easy to find that the PDBC predictions are closer to the analytical solutions than that of PD, regardless of the bond-based or the ordinary state-based constitutive model. In addition, Figs. 13 and 14 show that the displacement distribution of PDBC at the boundaries is more precise than that of PD, which indicates that the boundary effect of PD is more obvious.

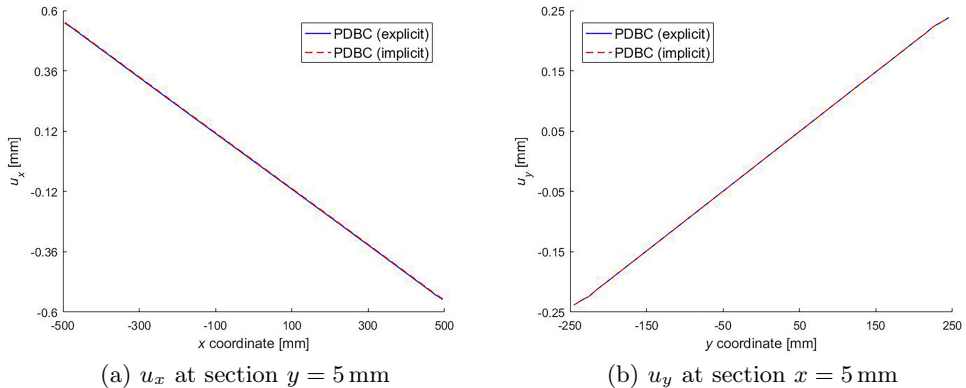


FIG. 9. Comparison of implicit with explicit algorithm based on the PM model.

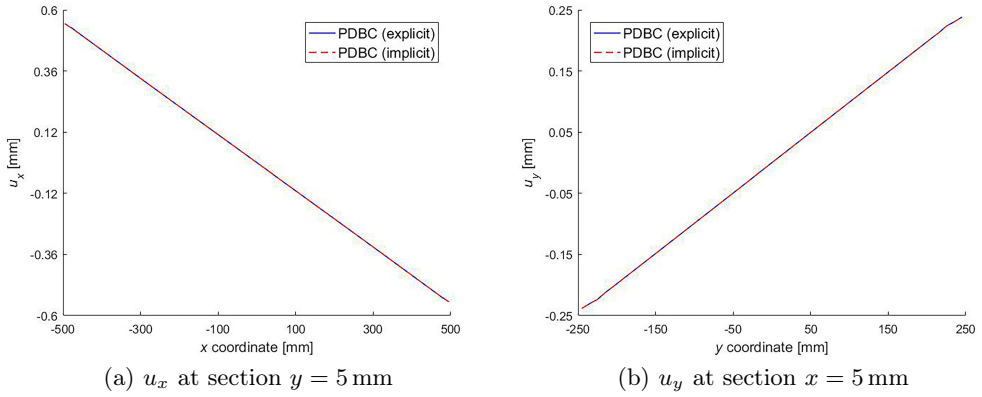


FIG. 10. Comparison of implicit with explicit algorithm based on the OSB model.

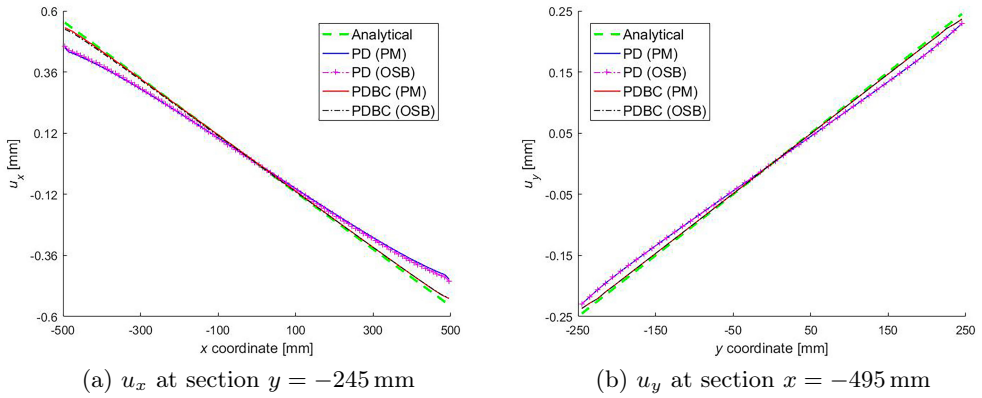


FIG. 11. The displacement at sections $y = -245$ mm and $x = -495$ mm in Example 1.

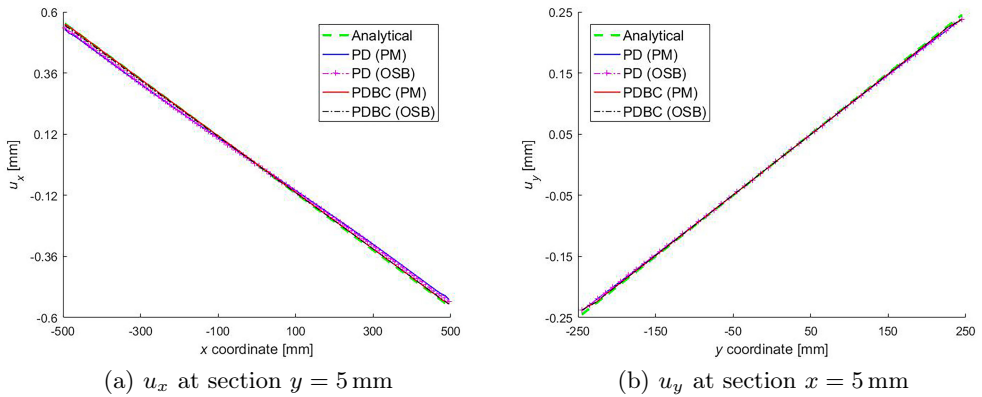


FIG. 12. The displacement at sections $y = 5$ mm and $x = 5$ mm in Example 1.

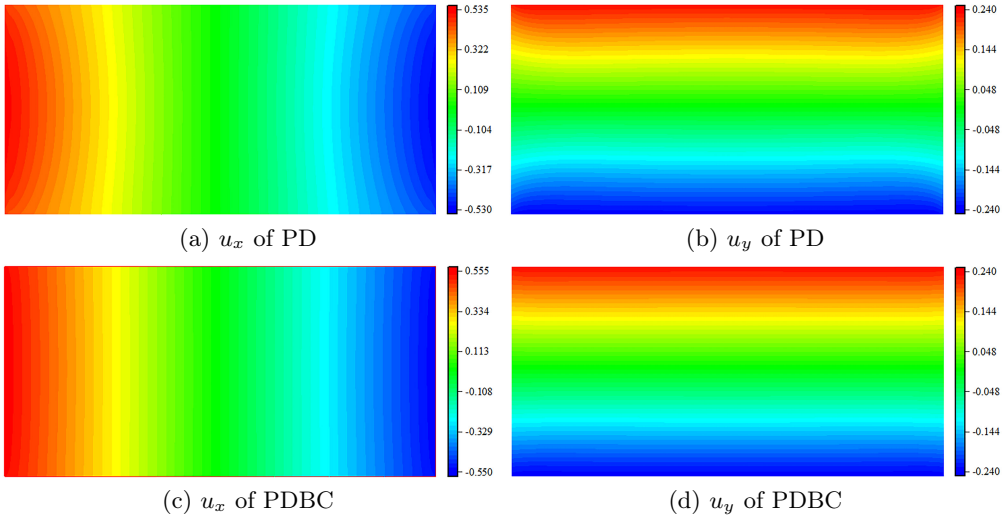


FIG. 13. The distribution of displacement based on the PM model in Example 1.

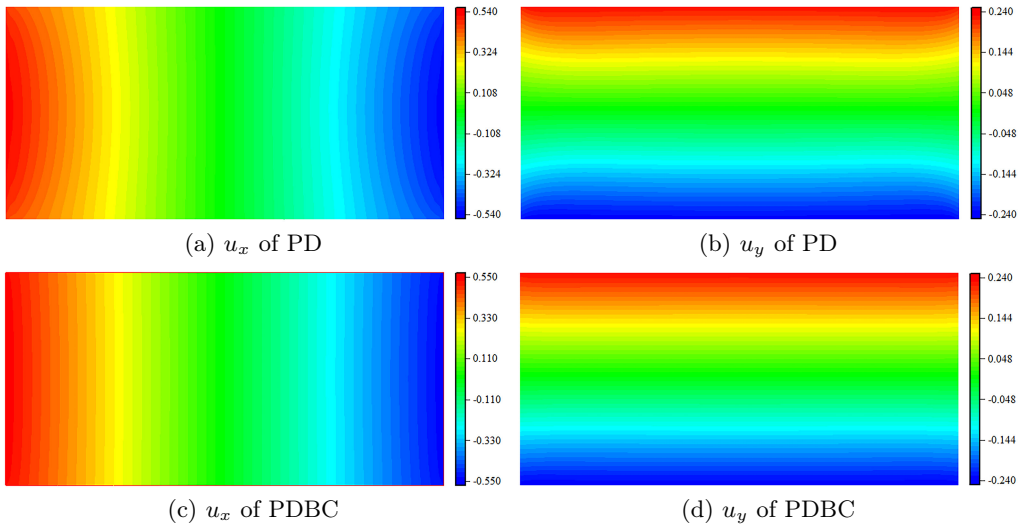


FIG. 14. The distribution of displacement based on the OSB model in Example 1.

5.2. Example 2: a cantilever rectangular plate with uniform compression

The cantilever rectangular plate is shown in Fig. 15. Its right side is subjected to uniform compression $q = 180$ MPa. Clearly, this is also a mixed boundary value problem, corresponding to Eq. (2.17) or Eq. (4.1).

Figures 16, 17 and 18 are the displacement contours in the cantilever plate calculated by FEM, PD and PDBC. They show that the displacements given

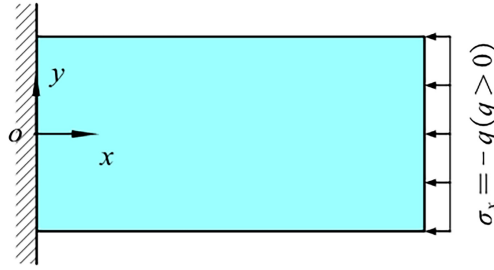


FIG. 15. Schematic diagram of subjected load of Example 2.

by PD and PDBC are quite close in distribution, and the relative error between them is within 3%, regardless of the bond-based or the ordinary state-based constitutive model. In x direction, although the relative errors between PDBC,

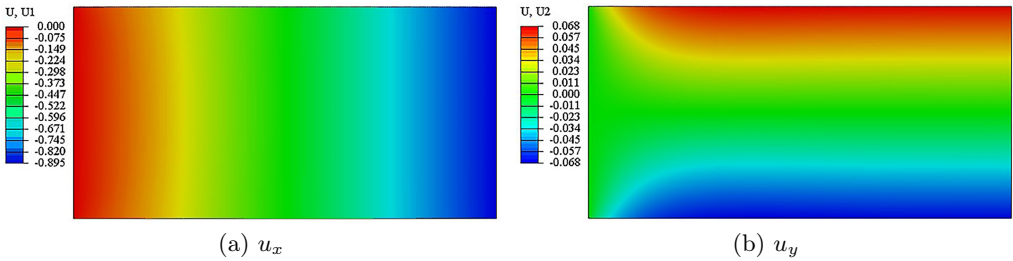


FIG. 16. The distribution of displacement obtained by ABAQUS in Example 2.

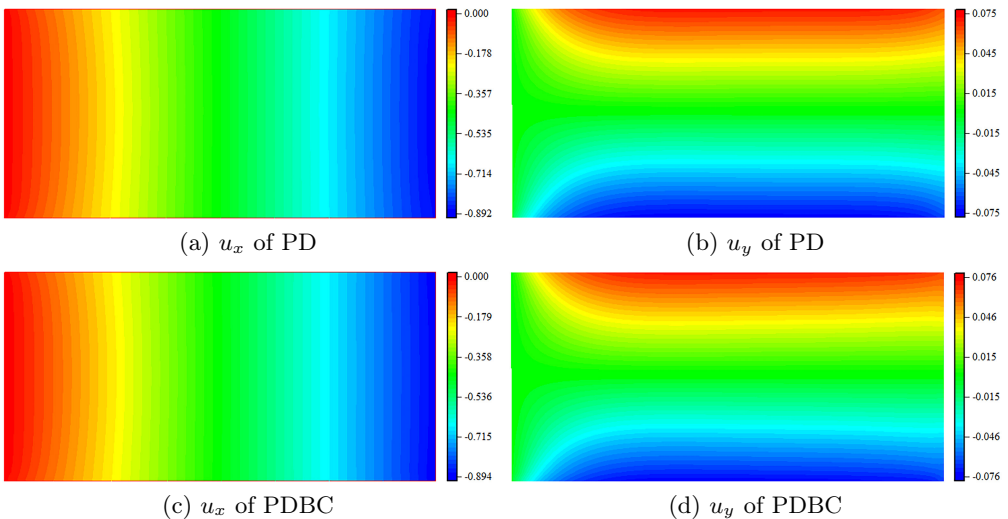


FIG. 17. The distribution of displacement based on the PM model in Example 2.

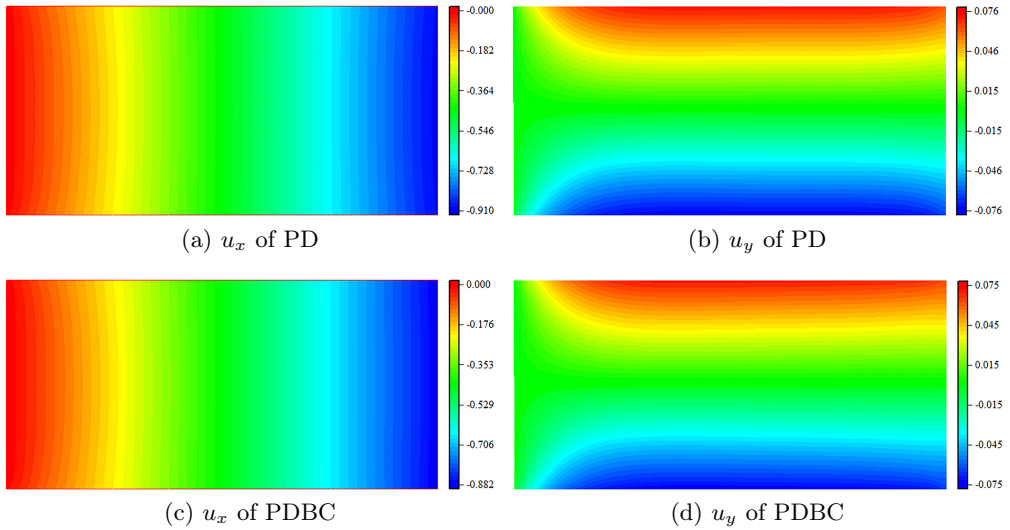


FIG. 18. The distribution of displacement based on the OSB model in Example 2.

PD and the FEM prediction are within 2%, the PDBC prediction is closer to the FEM prediction. The same is true in y direction, but the PDBC prediction is closer to the FEM prediction when the ordinary state-based constitutive model is used.

5.3. Example 3: a rectangular plate with the given displacements on all edges

As shown in Fig. 19, the displacement $U_0 = 0.45$ mm is applied on the two opposite edges of the rectangular plate in the x direction and $V_0 = 0.25$ mm on the other two edges in the y direction. Such a case forms a displacement boundary value problem, corresponding to Eq. (2.18) or Eq. (4.2).

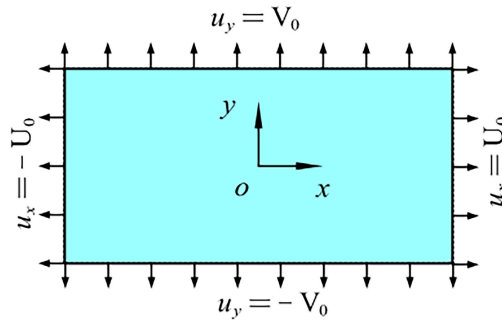


FIG. 19. Schematic diagram of subjected load of Example 3.

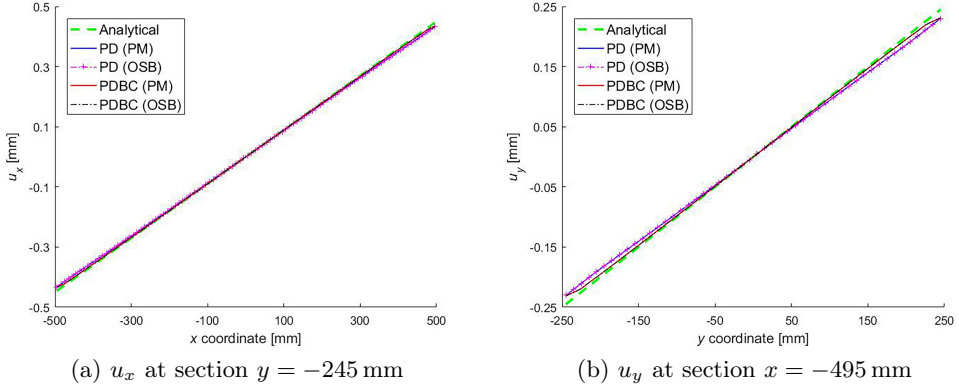


FIG. 20. The displacement at sections $y = -245$ mm and $x = -495$ mm in Example 3.

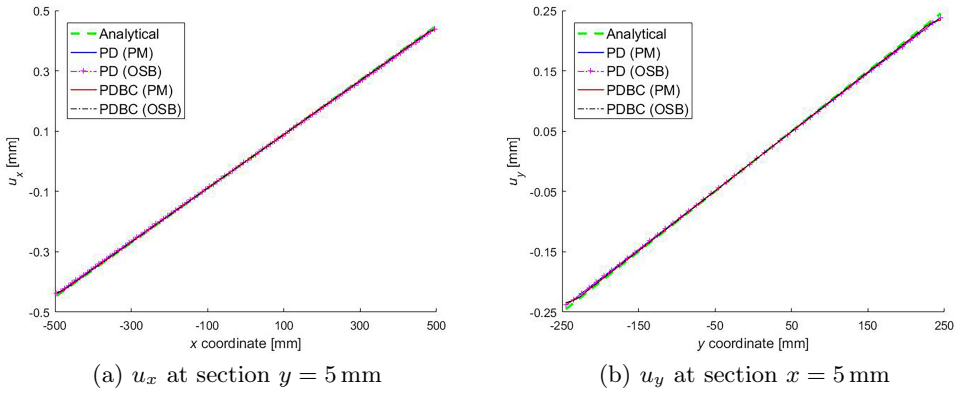


FIG. 21. The displacement at sections $y = 5$ mm and $x = 5$ mm in Example 3.

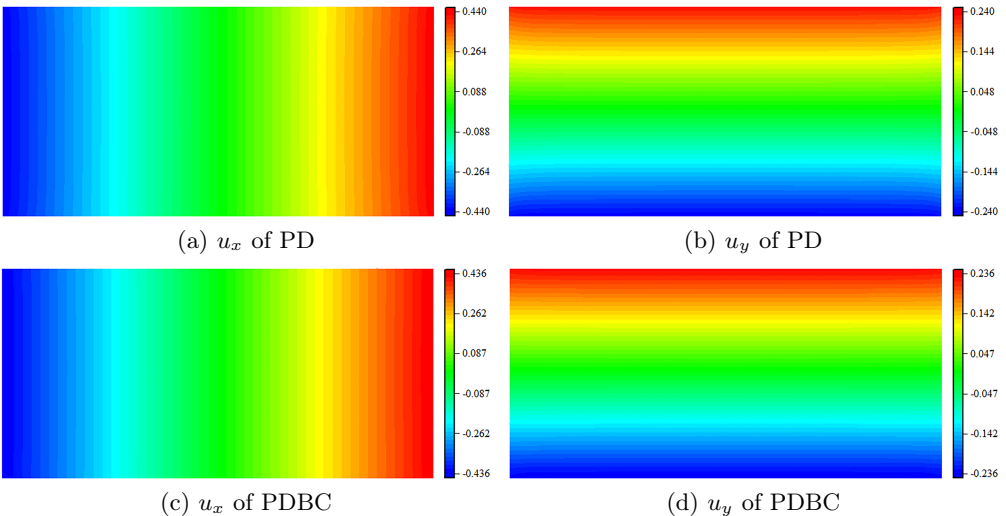


FIG. 22. The distribution of displacement based on the PM model in Example 3.

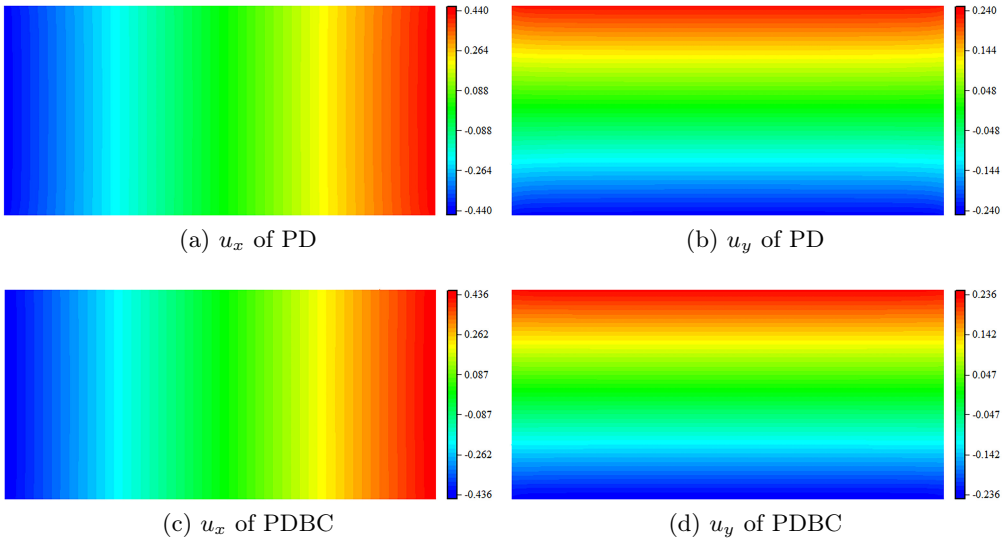


FIG. 23. The distribution of displacement based on the OSB model in Example 3.

From Figs. 20 to 23, we can find that although PDBC and PD predictions both are well matched with analytical solutions, the displacement distribution of PDBC at the boundaries is more exact than that of PD, regardless of whether the bond-based or the ordinary state-based constitutive model is used.

5.4. Example 4: a rectangular plate with two opposite edges subjected to tension

As shown in Fig. 24, the upper and lower edges of the rectangular plate are subjected to uniform tension $q = 200\text{MPa}$. Clearly, this is a traction boundary value problem, corresponding to Eq. (2.19) or Eq. (4.3).

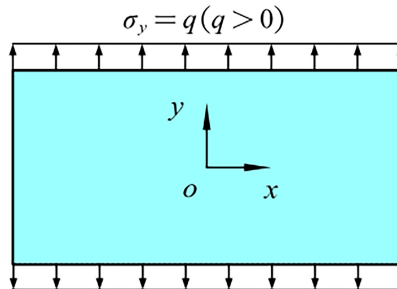


FIG. 24. Schematic diagram of subjected load of Example 4.

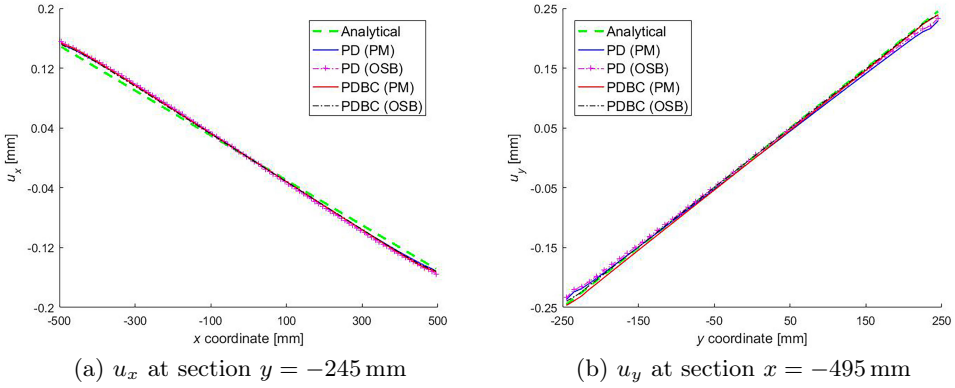


FIG. 25. The displacement at sections $y = -245$ mm and $x = -495$ mm in Example 4.

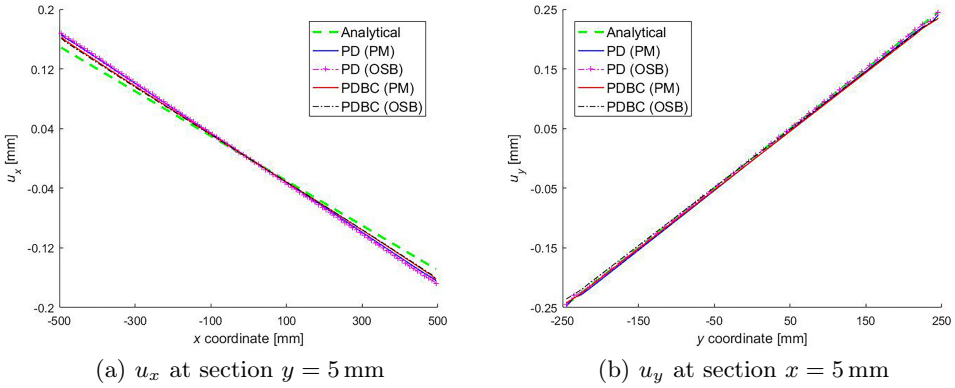


FIG. 26. The displacement at sections $y = 5$ mm and $x = 5$ mm in Example 4.

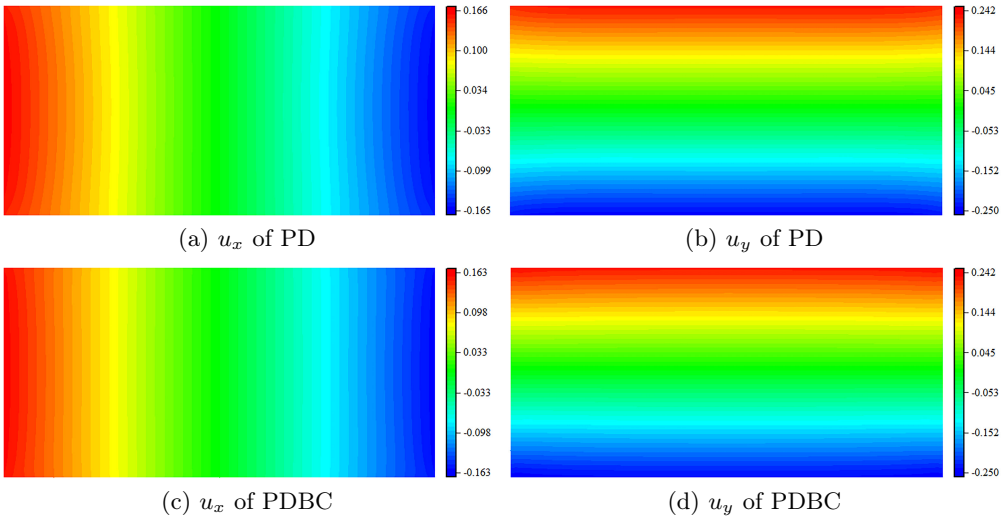


FIG. 27. The distribution of displacement based on the PM model in Example 4.

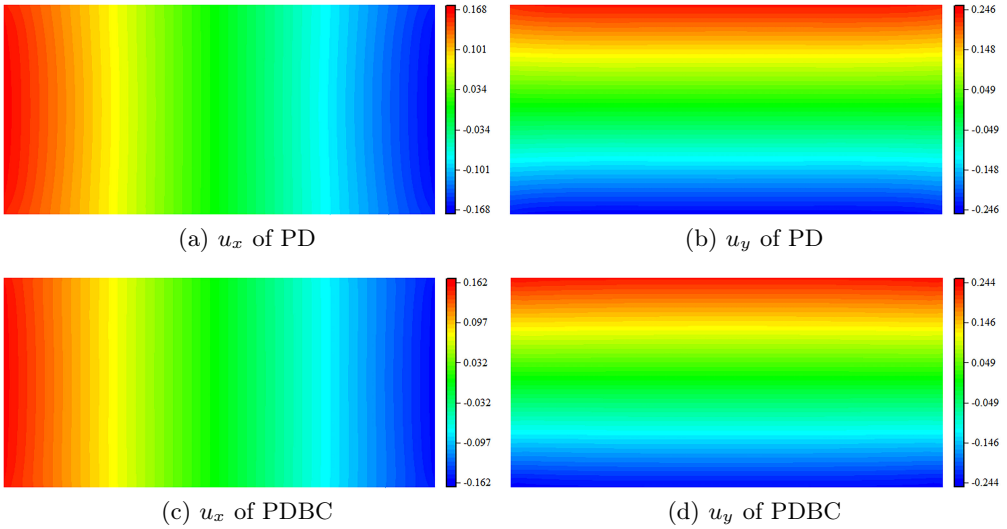


FIG. 28. The distribution of displacement based on the OSB model in Example 4.

It can be seen from Figs. 25 and 26 that the PDBC predictions are closer to the analytical solutions, regardless of the bond-based or the ordinary state-based constitutive model. In addition, Figs. 27 and 28 indicate that the displacement distribution of PDBC at the boundaries is more exact than that of PD.

5.5. Example 5: a rectangular plate subjected to bending

As shown in Fig. 29, the rectangular plate is subjected to an anti-symmetrically distributed linear loads with a maximal value $q = 200$ Mpa. As well known, this is a pure bending problem with the complicated traction boundary condition.

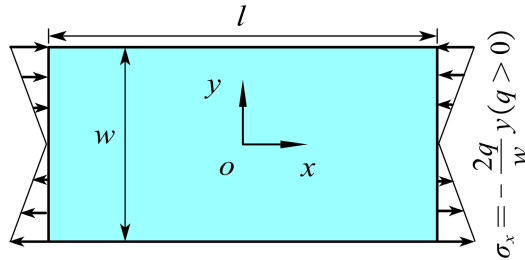
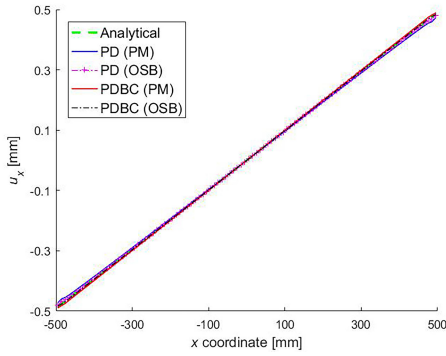
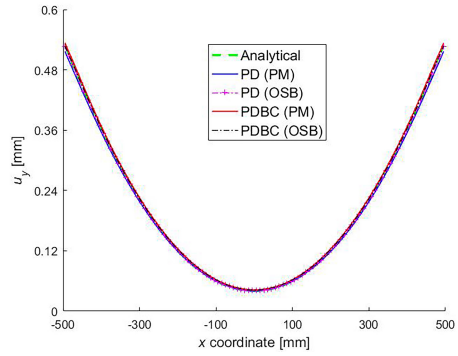


FIG. 29. Schematic diagram of subjected load of Example 5.

As can be seen from Figs. 30 to 35, the displacement distribution predicted by PDBC agrees with that by PD, and both of them agree well with the analytical solutions on the whole. The relative errors between them are less than 3%,

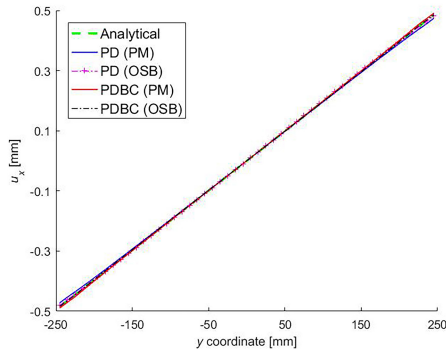


(a) u_x at section $y = -245$ mm

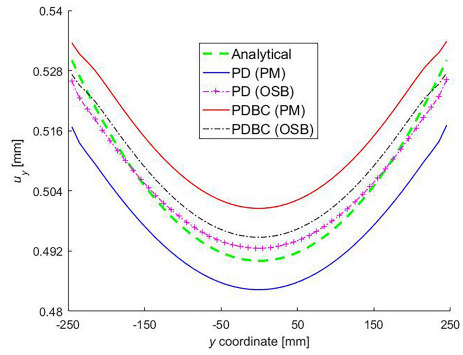


(b) u_y at section $y = -245$ mm

FIG. 30. The displacement at section $y = -245$ mm in Example 5.

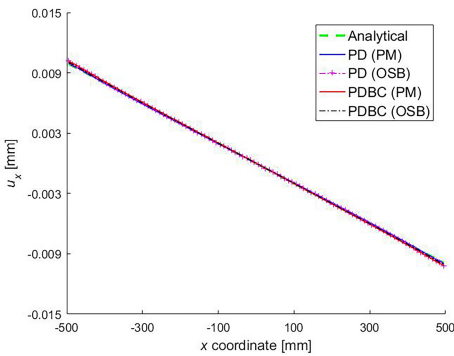


(a) u_x at section $x = -495$ mm

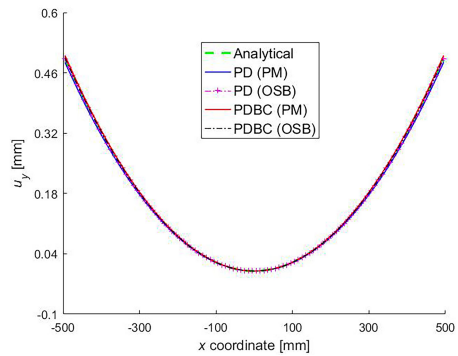


(b) u_y at section $x = -495$ mm

FIG. 31. The displacement at section $x = -495$ mm in Example 5.



(a) u_x at section $y = 5$ mm



(b) u_y at section $y = 5$ mm

FIG. 32. The displacement at section $y = 5$ mm in Example 5.

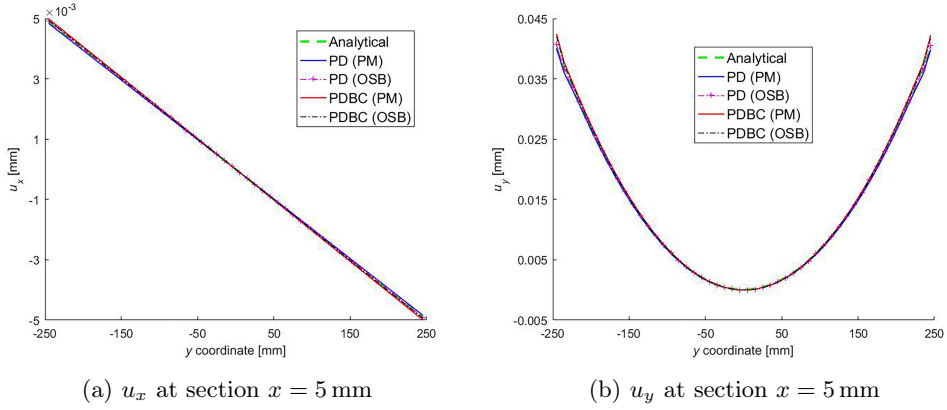


FIG. 33. The displacement at section $x = 5$ mm in Example 5.

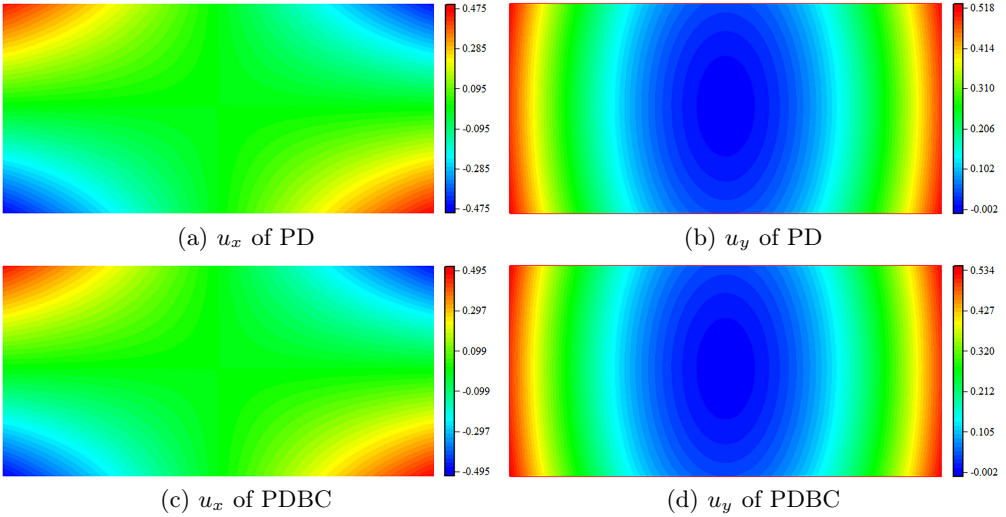


FIG. 34. The distribution of displacement based on the PM model in Example 5.

regardless of the bond-based or the ordinary state-based constitutive model. In addition, the prediction results of the ordinary state-based constitutive model are better than those of the bond-based constitutive model, regardless of PD or PDBC.

6. Conclusions

The new peridynamic equation of motion PDBC proposed in this paper is essentially an extension of the Silling peridynamic equation of motion. Through

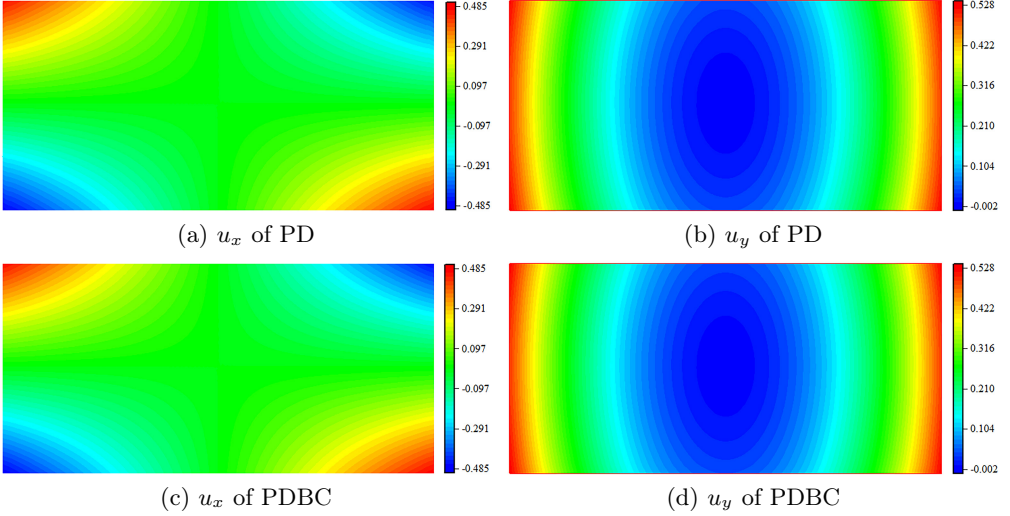


FIG. 35. The distribution of displacement based on the OSB model in Example 5.

calculating the benchmark examples of the plane stress problems, PDBC is verified to be efficacious for naturally handling the complex boundary conditions, and it does not require surface correction. The main conclusions are summarized as follows.

(1) The model parameter introduced in PDBC is determined by an equivalent assumption that elastic solutions for the displacements at the ends of a stretching rod are equal to the PD solutions regardless of the bond-based constitutive model or the ordinary state-based constitutive model.

(2) On the whole, the computational results for the benchmark problems by PDBC and PD are closed to each other, but the concept of traction and the traction boundary condition are preserved in PDBC.

(3) Compared with PD, PDBC does not need surface correction in the numerical calculation. It is more suitable for problems with complex boundary shapes.

Appendix A

To deal with boundary traction, the existing method transforms it into a body force, that is

$$(A.1) \quad \mathbf{b}_1(\mathbf{x}, t) = \begin{cases} \frac{\int_{\partial\Omega_p} \mathbf{p}(\mathbf{x}''', t) dA_{\mathbf{x}'''} }{V_B} & \text{for } \mathbf{x} \in \Omega_B, \\ \mathbf{0} & \text{otherwise,} \end{cases}$$

where Ω_B represents the boundary layer with $\partial\Omega_p$ as the boundary surface, and V_B is the volume of Ω_B .

Let $\partial\Omega_p = \partial\Omega$, and the body force $\mathbf{b}(\mathbf{x}, t)$ does not exist. Then, Eq. (2.1) can be rewritten as

$$(A.2) \quad \rho(\mathbf{x})\ddot{\mathbf{u}}(\mathbf{x}, t) = \int_{H_{\mathbf{x}}} \{\underline{\mathbf{T}}[\mathbf{x}, t]\langle \boldsymbol{\xi} \rangle - \underline{\mathbf{T}}[\mathbf{x}', t]\langle -\boldsymbol{\xi} \rangle\} dV_{\mathbf{x}'} + \mathbf{b}_1(\mathbf{x}, t).$$

Integrating Eq. (A.2) over Ω leads to

$$(A.3) \quad \int_{\Omega} \rho(\mathbf{x})\ddot{\mathbf{u}}(\mathbf{x}, t) dV_{\mathbf{x}} \\ = \int_{\Omega} \int_{H_{\mathbf{x}}} \{\underline{\mathbf{T}}[\mathbf{x}, t]\langle \boldsymbol{\xi} \rangle - \underline{\mathbf{T}}[\mathbf{x}', t]\langle -\boldsymbol{\xi} \rangle\} dV_{\mathbf{x}'} dV_{\mathbf{x}} + \int_{\Omega} \mathbf{b}_1(\mathbf{x}, t) dV_{\mathbf{x}}.$$

The first term at the right side of Eq. (A.3) is equal to zero [2]. Owing to Eq. (A.1), Eq. (A.3) reduces to

$$(A.4) \quad \int_{\Omega} \rho(\mathbf{x})\ddot{\mathbf{u}}(\mathbf{x}, t) dV_{\mathbf{x}} = \int_{\partial\Omega} \mathbf{p}(\mathbf{x}''', t) dA_{\mathbf{x}'''},$$

which shows that Eq. (A.2) satisfies the balance of total linear momentum.

However, when the balance of angular momentum is considered, we have

$$(A.5) \quad \int_{\Omega} \mathbf{y}(\mathbf{x}, t) \times \rho(\mathbf{x})\ddot{\mathbf{u}}(\mathbf{x}, t) dV_{\mathbf{x}} \\ = \int_{\Omega} \mathbf{y}(\mathbf{x}, t) \times \int_{H_{\mathbf{x}}} \{\underline{\mathbf{T}}[\mathbf{x}, t]\langle \boldsymbol{\xi} \rangle - \underline{\mathbf{T}}[\mathbf{x}', t]\langle -\boldsymbol{\xi} \rangle\} dV_{\mathbf{x}'} dV_{\mathbf{x}} + \int_{\Omega} \mathbf{y}(\mathbf{x}, t) \mathbf{b}_1(\mathbf{x}, t) dV_{\mathbf{x}}.$$

Owing to Eq. (A.1), the third term in Eq. (A.5) can be rewritten as

$$(A.6) \quad \int_{\Omega} \mathbf{y}(\mathbf{x}, t) \times \mathbf{b}_1(\mathbf{x}, t) dV_{\mathbf{x}} \\ = \frac{1}{V_B} \int_{\Omega_B} \mathbf{y}(\mathbf{x}, t) \times \int_{\partial\Omega} \mathbf{p}(\mathbf{x}''', t) dA_{\mathbf{x}'''} dV_{\mathbf{x}} \\ = \frac{1}{V_B} \int_{\Omega_B} \int_{\partial\Omega} \mathbf{y}(\mathbf{x}, t) \times \mathbf{p}(\mathbf{x}''', t) dA_{\mathbf{x}'''} dV_{\mathbf{x}} \\ = \frac{1}{V_B} \int_{\partial\Omega} \int_{\Omega_B} \mathbf{y}(\mathbf{x}, t) \times \mathbf{p}(\mathbf{x}''', t) dV_{\mathbf{x}} dA_{\mathbf{x}'''} \\ \neq \int_{\partial\Omega} \mathbf{y}(\mathbf{x}''', t) \times \mathbf{p}(\mathbf{x}''', t) dA_{\mathbf{x}'''} = \int_{\partial\Omega} \mathbf{y}(\mathbf{x}, t) \times \mathbf{p}(\mathbf{x}, t) dA_{\mathbf{x}}.$$

From Eq. (A.6), it can be seen that converting the traction force on the boundary surface into the body force within the boundary layer cannot guarantee that the angular momentum equilibrium is satisfied.

Appendix B

Let \mathbf{R} be the residual. The discrete equations Eq. (4.1), Eq. (4.2) and Eq. (4.3) can be in unified form represented as

$$(B.1) \quad \mathbf{R}(\mathbf{x}_i, \mathbf{u}_i, t) = \mathbf{e}\mathbf{f}(\mathbf{x}_i, \mathbf{u}_i, t) + \mathbf{i}\mathbf{f}(\mathbf{x}_i, \mathbf{u}_i, t) = \mathbf{0},$$

where $\mathbf{e}\mathbf{f}$ represents the external forces exerting at all nodes, and $\mathbf{i}\mathbf{f}$ the internal forces acting at all nodes. Taking Eq. (4.1) as an example, $\mathbf{e}\mathbf{f}$ and $\mathbf{i}\mathbf{f}$ in Eq. (B.1) can be written as

$$(B.2) \quad \left\{ \begin{array}{l} \mathbf{e}\mathbf{f}(\mathbf{x}_i, \mathbf{u}_i, t) = \chi \sum_{\partial\Omega_u} \{L(\mathbf{x}_i, \mathbf{x}_k)[\bar{\mathbf{y}}(\mathbf{x}_k, t) - \mathbf{y}(\mathbf{x}_i, t)]\} A_{\mathbf{x}_k} \\ \quad + \frac{\chi}{\chi - 1} \sum_{\partial\Omega_p} \{G(\mathbf{x}_i, \mathbf{x}_k)\bar{\mathbf{p}}(\mathbf{x}_k, t) + L(\mathbf{x}_i, \mathbf{x}_k)\mathbf{y}(\mathbf{x}_i, t)\} A_{\mathbf{x}_k} + \mathbf{b}(\mathbf{x}_i, t), \\ \mathbf{i}\mathbf{f}(\mathbf{x}_i, \mathbf{u}_i, t) = \sum_{H_{\mathbf{x}_i}} \{\mathbf{T}[\mathbf{x}_i, t]\langle \mathbf{x}_j - \mathbf{x}_i \rangle - \mathbf{T}[\mathbf{x}_j, t]\langle \mathbf{x}_i - \mathbf{x}_j \rangle\} V_{\mathbf{x}_j}. \end{array} \right.$$

In a perfectly equilibrated configuration, the residual vector \mathbf{R} is equal to $\mathbf{0}$. As a numerical algorithm, the Newton–Raphson method focuses on finding the approximation of the displacements \mathbf{u} at all nodes so that the configuration is closest to the equilibrium. Borrowing terminology from the nonlinear finite element method, we call the partial derivative $\partial\mathbf{R}/\mathbf{u}$ of residual \mathbf{R} with respect to displacements \mathbf{u} as the Jacobian matrix [41], denoted as \mathbf{A} , and the partial derivative $\partial\mathbf{i}\mathbf{f}/\mathbf{u}$ of an internal force $\mathbf{i}\mathbf{f}$ with respect to displacements \mathbf{u} as tangent stiffness matrix [41], denoted as \mathbf{K} . According to the iterative scheme of the Newton–Raphson method, we have

$$(B.3) \quad \begin{aligned} \frac{\partial\mathbf{R}}{\partial\mathbf{u}} \Big|_{\mathbf{u}^n} \cdot \Delta\mathbf{u} &= \frac{\partial\mathbf{R}(\mathbf{x}_i^n, \mathbf{u}_i^n, t)}{\partial\mathbf{u}^n} \cdot \Delta\mathbf{u} = \mathbf{A} \Big|_{\mathbf{u}^n} \cdot \Delta\mathbf{u} \\ &= -\mathbf{R} \Big|_{\mathbf{u}^n} = -\mathbf{R}(\mathbf{x}_i^n, \mathbf{u}_i^n, t), \end{aligned}$$

where $\Delta\mathbf{u} = \mathbf{u}^{n+1} - \mathbf{u}^n$ represents the increment of displacements \mathbf{u} of all nodes at iterative step $n+1$ and iterative step n . The increment of displacements can be obtained by solving the system of linear equations in Eq. (B.3), and then nodal displacements of iterative step $n+1$ can be obtained according to nodal displacements of iterative step n . Iteration can be stopped until a scalar value of residual \mathbf{R} , for example, l_2 -norm of \mathbf{R} has dropped below a specified threshold value. The specific steps of the Newton–Raphson method are as follows.

step 1: Initialize, $n = 0$, $\mathbf{u}_{\text{trial}} = \mathbf{0}$.

step 2: Apply the Newton–Raphson method to minimize the residual.

step 2-1: Evaluate the external force vector \mathbf{ef} , for $\mathbf{u}_{\text{trial}}$, if it needs to be updated.

step 2-2: Evaluate the residual vector \mathbf{R} , for $\mathbf{u}_{\text{trial}}$.

step 2-3: If the convergence criterion is met, that is $\|\mathbf{R}\| \leq 10^{-6}$, go to step 3; otherwise go to step 2-4.

step 2-4: Construct the Jacobian matrix \mathbf{A} of $\mathbf{u}_{\text{trial}}$.

step 2-5: Exert constraints, if necessary.

step 2-6: Solve the system of linear equations $\mathbf{A} \cdot \Delta \mathbf{u} = -\mathbf{R}$, obtained $\Delta \mathbf{u}$.

step 2-7: Set $\mathbf{u}_{\text{trial}} = \mathbf{u}_{\text{trial}} + \Delta \mathbf{u}$.

step 2-8: Set $n = n + 1$ and return to step 2-1.

step 3: Set $\mathbf{u} = \mathbf{u}_{\text{trial}}$.

It can be seen from Eq. (4.1) and Eq. (4.2) that the surface integral term in mixed boundary value problems and displacement boundary value problems is the function of nodal displacements. Therefore, the step 2-1 needs to be done for these two kinds of problems, while for traction boundary value problems, it is not required and we have $\mathbf{A} = \mathbf{K}$. The constraint handling in step 2-5 needs to be done for all problems involving the displacement boundary condition.

It can be seen from Eq. (B.3) that Jacobian matrix \mathbf{A} consisting of the tangent stiffness matrix \mathbf{K} and $\partial \mathbf{ef}/\mathbf{u}$ is necessary when the Newton–Raphson method is used to solve nonlinear problems. Eq. (4.1) and Eq. (4.2) show that $\partial \mathbf{ef}/\mathbf{u}$ can be easily obtained if the body force is ignored. As result, how to construct \mathbf{K} becomes the key.

For nonlinear constitutive models, the tangent stiffness matrix is a function of nodal displacements. Therefore, once the nodal displacements are updated, the tangent stiffness matrix must be re-evaluated. The tangent stiffness matrix is defined as

$$(B.4) \quad K_{sr} = \frac{\partial i f_s(\mathbf{x}_i, \mathbf{u}_i, t)}{\partial u_r},$$

where $i f_s$ is a component of the internal force vector \mathbf{if} , and u_r is a component of the displacements vector \mathbf{u} .

The construction of the tangent stiffness matrix includes analytical and computational approaches. Analytical approaches can refer to [18, 23, 42]. Computational approaches are more universal, and commonly used one is the finite-difference method [38, 39], in which a central-difference scheme used in place of Eq. (B.4) can be expressed as follows

$$(B.5) \quad K_{sr} \approx \frac{i f_s^{\mathbf{u}+\varepsilon_r}(\mathbf{x}_i, \mathbf{u}_i, t) - i f_s^{\mathbf{u}-\varepsilon_r}(\mathbf{x}_i, \mathbf{u}_i, t)}{2\varepsilon},$$

where $\boldsymbol{\varepsilon}_r$ is a perturbation displacement vector containing a single nonzero entry ε corresponding to the r^{th} displacement degree of freedom in the discretization, while $if_s^{u+\varepsilon r}$ is if_s with positive perturbation displacements $\boldsymbol{\varepsilon}_r$. For an accurate approximation, the magnitude of ε should be chosen to be small relative to the spacing between nodes after discretization, but not so small that the limitations of machine precision become a significant factor. The disturbance size ε is taken as 1.0×10^{-6} times the nodal spacing [38, 39] in this paper. The pseudocode of constructing the tangent stiffness matrix with the central-difference scheme is shown as follows.

- 1: Initialize, $\mathbf{K} = \mathbf{O}$.
- 2: for i do (traverse every discrete node).
- 3: for r do (traverse the displacement degree of freedom of node i).
- 4: A positive perturbation displacement is imposed at degree of freedom r of node i .
- 5: Evaluate internal force vector $\mathbf{f_pos}$ of all nodes under positive perturbation displacements.
- 6: A negative perturbation displacement is imposed at degree of freedom r of node i .
- 7: Evaluate internal force vector $\mathbf{f_neg}$ of all nodes under negative perturbation displacements.
- 8: for j do (traverse every discrete node).
- 9: for s do (traverse the displacement degree of freedom of node j).
- 10: $K(s^{\text{th}}, r^{\text{th}}) = K(s^{\text{th}}, r^{\text{th}}) + [\mathbf{f_pos}(s^{\text{th}}, 1) - \mathbf{f_neg}(s^{\text{th}}, 1)] / (2\varepsilon)$.
- 11: end for s .
- 12: end for j .
- 13: end for r .
- 14: end for i .

It should be emphasized that for the state-based constitutive model, the tangent stiffness matrix \mathbf{K} and the Jacobian matrix \mathbf{A} are asymmetric due to the bond force vectors having unequal magnitudes. If the coefficient matrix is asymmetric, some specialized methods such as generalized minimum residual method (GMRES) need to be used to solve the system of linear equations in Eq. (B.3).

Appendix C

As a benchmark example, the elastic displacement solution of a stretching rod is repeatedly verified by experimental results. Therefore, the PD solution should be at least the same as the elastic solution in terms of the total elongation of the stretched rod, i.e., the displacement at the end of the rod.

Consider a rod with the length of l and cross-sectional area of h_1 subjected to the tensile force F at two ends. Let the PM constitutive model characterized

by Eq. (3.7) be adopted and the coordinate origin be placed in the center of the rod. Substituting the elastic solution $u(x) = (F/h_1 E)x$ into Eq. (2.19) and then taking $x = l/2$, we have:

$$\begin{aligned}
 \text{(C.1)} \quad \frac{\chi}{\chi-1} G\left(\frac{l}{2}, \frac{l}{2}\right) F + ch_1 \frac{F}{h_1 E} \int_{l/2-\delta}^{l/2} \frac{x' - \frac{l}{2}}{|x' - \frac{l}{2}|} dx' &= 0 \\
 \Rightarrow \frac{\chi}{\chi-1} \frac{F}{\delta \ln 2 h_1} + \frac{2E}{h_1 \delta^2} h_1 \frac{F}{h_1 E} (-\delta) &= 0 \\
 \Rightarrow \frac{\chi}{\chi-1} &= 2 \ln 2.
 \end{aligned}$$

In terms of (C.1), we obtain $\chi = 2 \ln 2 / (2 \ln 2 - 1) = 3.59$, which is used in all calculations in this paper.

Acknowledgments

The support of the National Natural Science Foundation of China through the Grant Nos. 12072145 and 11672129 is gratefully acknowledged.

References

1. S.A. SILLING, *Reformulation of elasticity theory for discontinuities and long-range forces*, Journal of the Mechanics and Physics of Solids, **48**, 175–209, 2000.
2. S.A. SILLING, M. EPTON, O. WECKNER, J. XU, E. ASKARI, *Peridynamic states and constitutive modeling*, Journal of Elasticity, **88**, 151–184, 2007.
3. S.A. SILLING, M. ZIMMERMANN, R. ABEYARATNE, *Deformation of a peridynamic bar*, Journal of Elasticity, **73**, 173–190, 2003.
4. S.A. SILLING, E. ASKARI, *A meshfree method based on the peridynamic model of solid mechanics*, Computers and Structures, **83**, 1526–1535, 2005.
5. P. SELESON, M.L. PARKS, *On the role of the influence function in the peridynamic theory*, International Journal of Multiscale Computational Engineering, **9**, 689–706, 2011.
6. S.A. SILLING, R.B. LEHOUCQ, *Convergence of peridynamics to classical elasticity theory*, Journal of Elasticity, **93**, 13–37, 2008.
7. F. BOBARU, W. HU, *The meaning, selection, and use of the peridynamic horizon and its relation to crack branching in brittle materials*, International Journal of Fracture, **176**, 215–222, 2012.
8. R.W. MACEK, S.A. SILLING, *Peridynamics via finite element analysis*, Finite Elements in Analysis and Design, **43**, 1169–1178, 2007.
9. E. MADENCI, M. DORDUNCU, A. BARUT, N. PHAN, *Weak form of peridynamics for non-local essential and natural boundary conditions*, Computer Methods in Applied Mechanics and Engineering, **337**, 598–631, 2018.

10. E. MADENCI, M. DORDUNCU, N. PHAN, X. GU, *Weak form of bond-associated non-ordinary state-based peridynamics free of zero energy modes with uniform or non-uniform discretization*, Engineering Fracture Mechanics, **218**, 106613, 2019.
11. Z.X. HUANG, *Revisiting the peridynamic motion equation due to characterization of boundary conditions*, Acta Mechanica Sinica, **35**, 972–980, 2019.
12. Z. ZHOU, M. YU, X. WANG, Z. HUANG, *Peridynamic analysis of 2-dimensional deformation and fracture based on an improved technique of exerting traction on boundary surface*, Archives of Mechanics, **74**, 441–461, 2022.
13. M. YU, Z. ZHOU, Z. HUANG, *Traction-associated peridynamic motion equation and its verification in the plane stress and fracture problems*, Materials, **16**, 2252, 2023.
14. F. SCABBIA, M. ZACCARIOTTO, U. GALVANETTO, *A novel and effective way to impose boundary conditions and to mitigate the surface effect in state-based peridynamics*, International Journal for Numerical Methods in Engineering, **122**, 5773–5811, 2021.
15. F. SCABBIA, M. ZACCARIOTTO, U. GALVANETTO, *A new method based on Taylor expansion and nearest-node strategy to impose Dirichlet and Neumann boundary conditions in ordinary state-based peridynamics*, Computational Mechanics, **70**, 1–27, 2022.
16. O. WECKNER, G. BRUNK, M.A. EPTON, S.A. SILLING, E. ASKARI, *Green's functions in non-local three-dimensional linear elasticity*, Proceedings of the Royal Society A, **465**, 3463–3487, 2009.
17. Y. MIKATA, *Analytical solutions of peristatic and peridynamic problems for a 1D infinite rod*, International Journal of Solids and Structures, **49**, 2887–2897, 2012.
18. Y. HU, *Peridynamic modeling of fiber-reinforced composites with polymer and ceramic matrix*, Doctoral dissertation, University of Arizona, 2017.
19. S.A. SILLING, *Dynamic fracture modeling with a meshfree peridynamic code*, Computational Fluid and Solid Mechanics, 641–644, 2003.
20. B. KILIC, E. MADENCI, *An adaptive dynamic relaxation method for quasi-static simulations using the peridynamic theory*, Theoretical and Applied Fracture Mechanics, **53**, 194–204, 2010.
21. Y.D. HA, *An extended ghost interlayer model in peridynamic theory for high-velocity impact fracture of laminated glass structures*, Computers and Mathematics with Applications, **80**, 744–761, 2020.
22. M.L. PARKS, P. SELESON, S.J. PLIMPTON, S.A. SILLING, *Peridynamics with LAMMPS: a user guide v 0.3 beta*, Sandia Report, 2011–8253, 2011.
23. J.A. MITCHELL, *A nonlocal, ordinary, state-based plasticity model for peridynamics*, Sandia Report, SAND2011-3166, 2011.
24. J.A. MITCHELL, *A non-local, ordinary-state-based viscoelasticity model for peridynamics*, Sandia Report, SAND2011-8064, 2011.
25. N.A. HASHIM, W.M. COOMBS, C.E. AUGARDE, G. HATTORI, *An implicit non-ordinary state-based peridynamics with stabilised correspondence material model for finite deformation analysis*, Computer Methods in Applied Mechanics and Engineering, **371**, 113304, 2020.

26. L. LOPEZ, S.F. PELLEGRINO, *A space-time discretization of a nonlinear peridynamic model on a 2D lamina*, Computers and Mathematics with Applications, **116**, 161–175, 2022.
27. W. GERSTLE, N. SAU, S. SILLING, *Peridynamic modeling of concrete structures*, Nuclear Engineering and Design, **237**, 1250–1258, 2007.
28. X. CHEN, M. GUNZBURGER, *Continuous and discontinuous finite element methods for a peridynamics model of mechanics*, Computer Methods in Applied Mechanics and Engineering, **200**, 1237–1250, 2011.
29. M. ZINGALES, M.D. PAOLA, G. INZERILLO, *The finite element method for the mechanically based model of non-local continuum*, International Journal for Numerical Methods in Engineering, **86**, 1558–1576, 2011.
30. F. HAN, G. LUBINEAU, Y. AZDOUD, A. ASKARI, *A morphing approach to couple state-based peridynamics with classical continuum mechanics*, Computer Methods in Applied Mechanics and Engineering, **301**, 336–358, 2016.
31. Y. AZDOUD, F. HAN, G. LUBINEAU, *The morphing method as a flexible tool for adaptive local/non-local simulation of static fracture*, Computational Mechanics, **54**, 711–722, 2014.
32. Z.B. LI, F. HAN, *The peridynamics-based finite element method (PeriFEM) with adaptive continuous/discrete element implementation for fracture simulation*, Engineering Analysis with Boundary Elements, **146**, 56–65, 2023.
33. S.A. SILLING, R.B. LEHOUCQ, *Peridynamic theory of solid mechanics*, Advances in Applied Mechanics, **44**, 73–168 2010.
34. F. BOBARU, J.T. FOSTER, P.H. GEUBELLE, S.A. SILLING, *Handbook of Peridynamic Modeling*, CRC Press, Boca Raton, 2016.
35. E. MADENCI, E. OTERKUS, *Peridynamic Theory and Its Applications*, Springer, New York, 2014.
36. E. MADENCI, S. OTERKUS, *Ordinary state-based peridynamics for plastic deformation according to von Mises yield criteria with isotropic hardening*, Journal of the Mechanics and Physics of Solids, **86**, 192–219, 2016.
37. B. KILIC, *Peridynamic theory for progressive failure prediction in homogeneous and heterogeneous materials*, Doctoral dissertation, University of Arizona, 2008.
38. M.L. PARKS, D.J. LITTLEWOOD, J.A. MITCHELL, S.A. SILLING, *Peridigm users' guide v1.0.0*, Sandia Report, 2012-7800, 2012.
39. D.J. LITTLEWOOD, *Roadmap for peridynamic software implementation*, Sandia Report, 2015-9013, 2015.
40. F. BOBARU, M. YANG, L.F. ALVES, S.A. SILLING, E. ASKARI, J. XU, *Convergence, adaptive refinement, and scaling in 1D peridynamics*, International Journal for Numerical Methods in Engineering, **77**, 852–877, 2009.
41. T. BELYTSCHKO, W.K. LIU, B. MORAN, K. ELKHODARY, *Nonlinear Finite Elements for Continua and Structures*, 2nd ed., Ringgold Inc, Beaverton, 2014.
42. S.A. SILLING, *Linearized theory of peridynamic states*, Journal of Elasticity, **99**, 85–111, 2010.

43. T. BODE, C. WEISSENFELS, P. WRIGGERS, *Peridynamic Galerkin method: an attractive alternative to finite elements*, Computational Mechanics, **70**, 723–743, 2022.
44. D. BEHERA, P. ROY, S.V.K. ANICODE, E. MADENCI, B. SPENCER, *Imposition of local boundary conditions in peridynamics without a fictitious layer and unphysical stress concentrations*, Computer Methods in Applied Mechanics and Engineering, **393**, 114734, 2022.
45. Z.X. HUANG, *Peridynamic equation with boundary traction*, Journal of Mechanics of Materials and Structures, **18**, 675–683, 2023.

Received July 8, 2023; revised version January 3, 2024.

Published online February 23, 2024.
